LEVEL

ANALYSIS OF ULTRAVIOLET AND VISIBLE LASER EFFECTS

C. Duzy, C. J. Knight, J. A. Woodroffe, and L. A. Young

Avco Everett Research Laboratory, Inc.

a Subsidiary of Avco Corporation

2385 Revere Beach Parkway

Everett, MA 02149

January 1981

Final Technical Report for Period 20 August 1980 — 15 November 1980

APPROVED FOR PUBLIC RELEASE; DISTRIBUTION UNLIMITED.

81 2 09 120

FOREWORD

DARPA Order No.:   3643

Name of Contractor: Avco Everett Research Laboratory, Inc.

Effective Date of Contract: 8/20/80

Contract Expiration Date: 11/15/80

Reporting Period: 8/20/80 - 11/15/80

Contract No.:   DAAH01-80-C-1523

Principal Investigator and Phone No.:   J.A. Woodroffe
(617) 389-3000, Ext. 717

Short Title of Work: Analysis of Ultraviolet and Visible Laser
Effects

REPORT DOCUMENTATION PAGE

READ INSTRUCTIONS BEFORE COMPLETING FORM

1. REPORT NUMBER	**2. GOVT ACCESSION NO.** AD-A094787
3. RECIPIENT'S CATALOG NUMBER	

4. TITLE (and Subtitle)
Analysis of Ultraviolet and Visible Laser Effects

5. TYPE OF REPORT & PERIOD COVERED
Final Technical Report.
20 Aug 1980-15 Nov 1980

6. PERFORMING ORG. REPORT NUMBER

7. AUTHOR(s)
C. Duzy, C.J. Knight, J.A. Woodroffe, and L.A. Young

8. CONTRACT OR GRANT NUMBER(s)
DAAH01-80-C-1523
DARPA Order-3643

9. PERFORMING ORGANIZATION NAME AND ADDRESS
Avco Everett Research Laboratory, Inc.
2385 Revere Beach Parkway
Everett, Massachusetts 02148

10. PROGRAM ELEMENT, PROJECT, TASK AREA & WORK UNIT NUMBERS

11. CONTROLLING OFFICE NAME AND ADDRESS
Defense Advanced Research Projects Agency (DOD) DARPA Order No. 3643

12. REPORT DATE
January 1981

13. NUMBER OF PAGES
71

14. MONITORING AGENCY NAME & ADDRESS(if different from Controlling Office)
U. S. Army Missile Command
Redstone Arsenal, AL 35809

15. SECURITY CLASS. (of this report)
Unclassified

15a. DECLASSIFICATION/DOWNGRADING SCHEDULE

16. DISTRIBUTION STATEMENT (of this Report)

Approved for Public Release; Distribution Unlimited

17. DISTRIBUTION STATEMENT (of the abstract entered in Block 20, if different from Report)

18. SUPPLEMENTARY NOTES

19. KEY WORDS (Continue on reverse side if necessary and identify by block number)

UV/visible, laser effects, plasmas, vaporization

20. ABSTRACT (Continue on reverse side if necessary and identify by block number)

In extrapolating UV/visible effects data obtained with small spots to large spots, it is essential to determine the dominant mechanisms. In this report we present analytical results on the dominant effects at high fluence, vaporization of the surface and plasma formation. Under vacuum conditions with an aluminum surface and ~μs pulses, we find the impulse coupling coefficient due to vapor recoil to be ~3 for XeF and ~6 for KrF at high fluences. The plasma threshold is >25 MW/cm^2 incident flux and <100 MW/cm^2; the

DD FORM 1473 EDITION OF 1 NOV 65 IS OBSOLETE

20. ABSTRACT

exact value depends on assumptions regarding rate constants,

TABLE OF CONTENTS

1

LIST OF ILLUSTRATIONS

I. SUMMARY

A. INTRODUCTION

While a great deal of work has been done on laser effects with pulsed infrared lasers,[1] only recently have UV lasers of suitable energy levels been developed.[2] In the IR, the interaction between a pulsed laser and an aluminum surface in air is dominated by the formation of a plasma, which totally absorbs the laser energy. The plasma then re-radiates a large fraction of this energy in the UV. Since aluminum is a very good reflector in the IR, but a good absorber in the UV, this leads to higher surface coupling than would be the case if the plasma were absent. In addition, the plasma generates a significant impulse level on the target by remaining at high pressure for a significant period of time. With a UV laser, where the photons are much more energetic and where the basic absorptivity of the surface is higher, the phenomenology may be different.

Under IRAD funding, AERL measured the thermal coupling of KrF (249 nm) and XeF (353 nm) laser radiation to metal targets,

1. McKay, J.A., Schriempf, J.T., Cronburg, T.L., Eninger, J.E., and Woodroffe, J.A., "Pulsed CO_2 Laser Interaction with a Metal Surface at Oblique Incidence," Appl. Phys. Lett. <u>36</u> 125 (1980).

2. Jacob, J.H., Hsia, J.C., Mangano, J.A. and Ronki, M.J., Appl. Phys. <u>50</u>, 5130 (1979).

as well as the impulse coupling.[3,4] These results indicated
that damage by UV lasers should be very efficient. Similar
results have been obtained by other groups.[5,6]

All of the experiments to date have been with relatively
low pulse energy lasers. As a result, measurements at high
fluence have been carried out with small spots. In extrapolat-
ing to a large spot situation, it is important to determine what
are the dominant physical effects. The spot-size scaling will
be very different, for instance, if the phenomena at high fluence
are purely vapor dominated, as opposed to plasma dominated.

This report covers work performed under a DARPA-funded
program for Analysis of UV/Visible Laser Effects Data. The pur-
pose of the program was to determine what effects are important
at high fluence levels ($> 10 \, J/cm^2$), to help determine spot size
scaling. This knowledge is required for extrapolation to system
level energies and for proper design of damage experiments on
larger machines. Specifically, the program focused on two key
aspects: a) transient vaporization of aluminum into vacuum;
and b) plasma formation in aluminum vapor at the temperature and
density predicted by (a).

3. Woodroffe, J.A., Hsia, J. and Ballantyne, A., "Thermal and
   Impulse Coupling to an Aluminum Surface by a Pulsed KrF Laser,"
   Appl. Phys. Lett. 36, 14 (1980).

4. Duzy, C., Woodroffe, J.A., Hsia, J. and Ballantyne, A.,
   "Interaction of a Pulsed XeF Laser with an Aluminum Surface,"
   Appl. Phys. Lett. 37, 542 (1980).

5. Rosen, D.I., Mittledorf, J., Kothandaraman, G., Pirri, A.N.,
   and Pugh, E.R., AIAA Paper No. AIAA-80-1321, presented at 13th
   Fluid Plasma Dynamics Conference, Snowmass, Colorado, July 1980.

6. Walters, C.T., "Ultraviolet Laser Effects Experiment," Report
   No. BCL-G7029, Battelle Columbus Laboratories, Columbus, Ohio
   (1980).

This report is divided into three sections and an appendix. Section I presents the rationale for the choice of tasks (a) and (b)) and contains a summary description of the conclusions of the work described in the other two sections. Section II describes a calculation for vaporization of aluminum into a vacuum under conditions where steady state may or may not be reached. Section III presents a calculation for plasma formation in aluminum vapor. Finally, Appendix A contains a description of the AERL IRAD work on KrF and XeF laser effects.

B. RATIONALE

At low incident fluence levels (<1 J/cm^2), the interaction between the UV laser light and the surface results simply in warming up of the surface (see Appendix A). As the fluence increases, the phenomenology changes. First, isolated surface defects may reach the vaporization point, resulting in the appearance of impulse. Next the surface melts in bulk during the pulse. At still higher levels (~10-30 J/cm^2) the surface reaches the vaporization temperature during the pulse. At this point significant impulse levels appear. The impulse is expressed in terms of the coupling coefficient C, which represents the amount of impulse intensity (dyn-sec/cm^2) obtained per unit of fluence (J/cm^2). At the same time, the thermal coupling (expressed in terms of α, the ratio of energy left in the target after the pulse to the incident energy) begins to go down because the vapor carries away with it a great deal of energy. The vaporization process is transient, since the surface is heating up throughout the pulse.

Finally, at very high fluence ($>>30$ J/cm^2) two phenomena are dominant: strong (near steady-state) vaporization, and plasma formation. A plasma may form before or after strong vaporization begins. In the strong vaporization regime, high values of C ($\sim$3-10 dyn-sec/J) are observed (see Appendix A). If no plasma is formed, then the effect of spot size scaling is small. Because the temperatures are low and therefore the sound speeds are low, information about the existence of spot edges propagates slowly to the center of the spot (speed $\sim$1.5x10 cm/sec). Rather small spots (<1 cm^2 area for a pulse length $\sim$ 2μ sec) are suitable for near one-dimensional experiments. The results can then be easily extrapolated to the fully one-dimensional situation at operational energies.

If a vapor plasma is formed, however, then it can result in values of C much greater than 10 dyn-sec/J, and can also result in higher thermal coupling to the surface (as has been observed in the IR, for both impulse[7] and thermal coupling[8]). In the IR, the plasma medium is ambient air. In the UV, however, the principal interest is in vacuum interaction. Plasma formation and behavior are then much more complex, since the medium (vapor) has varying initial density and temperature. If a plasma is formed, the temperatures and sound speeds are much

7. Reilly, J., Ballantyne, A., Woodroffe, J.A., "Modelling of Momentum Transfer to a Surface by Laser Supported Absorption Waves," AIAA J. 17, 1098 (1979).

8. Pirri, A.N., Root, R.C.and Wu, P.K.S., "Plasma Energy Transfer to Metal Surfaces Irradiated by Pulsed Lasers," AIAA J. 16, 1296 (1978).

greater, resulting in an order of magnitude bigger spot size requirements for near one-dimensional experiments.

Given the interest in extrapolating to very high fluences and large spots, we chose to perform analyses on (a) the transient vaporization process to determine impulse levels if only vaporization is important, and to obtain initial vapor conditions as a function of incident flux; and (b) plasma formation time in aluminum vapor, for the initial conditions obtained from the vaporization calculations. With the latter information, we can then determine whether a plasma will be present or not at a particular flux. A task that remains for future work is the integration of the two analyses to obtain a predictive capability for the surface/vapor/plasma system for both thermal and impulse coupling.

C. SUMMARY OF CONCLUSIONS

The two analyses are described fully in Sections II and III. Only the conclusions will be given here.

1. Section II, Transient Vaporization

   1) Generally, heat conduction into the bulk metal and vapor efflux represent equally important mechanisms for removing absorbed power from the surface or vapor interface.

2) The surface heat up time varies inversely with the square of the absorbed power and becomes small compared to the incident pulse duration at incident XeF fluxes $\gtrsim 100$ MW/cm^2.

3) The impulse coupling coefficient C is one parameter relevant to understanding damage mechanisms associated with pulsed devices interacting with a surface. At 100 MW/cm^2 absorbed and 1 µsec, C ~ 3 for α ~ 20% (XeF) and ~6 for α ~40% (KrF), corresponding to an incident fluence of 500 J/cm^2 and 250 J/cm^2, respectively.

2. Section III, Plasma Formation

1) Plasma formation was not predicted at an incident flux of 25 MW/cm^2 for any of the sets of rate constants considered in this work, while at 100 MW/cm^2 plasma was formed very rapidly regardless of the assumptions used in determining the rate constants. Between the two extremes, the relative magnitude of the photoionization and electron impact ionization rates determined whether a plasma is present.

2) Experiments with 1-2 µsec pulses at high fluences (>100 J/cm^2) will be in the plasma regime and therefore large spots and a laser with large pulse energy are necessary to do the required one-dimensional experiments.

10

3) Several improvements can be made in the model, such as: inclusion of a non-Maxwellian electron distribution for determining the electron impact rate constants; a better estimate for electron impact ionization; a more detailed calculation for the photo-ionization cross section from the 4p state of aluminum.

4) Re-radiation from the plasma while probably a small effect needs to be included in the model in future work.

II. TRANSIENT VAPORIZATION FROM A SURFACE INTO VACUUM

A. INTRODUCTION

It is possible to direct energy into a surface at high power density (e.g., $\gtrsim 1$ MW/cm^2) and thereby induce rapid surface vaporization. High power lasers represent one such energy source. There have been several studies of the ensuing processes when there is a surrounding air environment [7,8,3]. The case of a surface initially surrounded by a hard vacuum is less well studied and is the object of this section. The external energy source is taken to be pulsed and absorbed only at the surface (or phase interface with the vapor flow region). Absorption in the vapor phase is not considered even though it can be important in processes such as laser-induced breakdown.[9,10] That represents a separate process which will be pursued in Section III.

The basic methodology to be outlined is fairly general, but it is convenient to choose a particular material in order to render the discussion more concrete. An aluminum surface will be considered herein. The primary mechanisms for removing the absorbed power from the surface are typically heat conduction into the dense phase behind the surface and efflux of vapor from the

9. Shui, V., Kivel, B. and Weyl, G., "Effect of Vapor Plasma on the Coupling of Laser Radiation with Aluminum Targets," J. Quantum Spectroscopy and Radiative Transfer 20, 627, (1978).

10. Weyl, G., Pirri, A., Root, R., "Laser Ignition of Plasma Off Aluminum Surfaces," AIAA-80-1319, 13th Fluid and Plasma Dynamics Conference, July 1980.

AVCO EVERETT

surface, carrying with it the heat of vaporization. Theoretical modeling of these two processes will be discussed in turn. Then the discussion will proceed to coupling them with the transient vapor flow away from the surface.

B. MODEL

At the absorbed power fluxes of interest ($\gtrsim 1$ MW/cm^2), the aluminum surface will very quickly heat up to a temperature well above the melting point. Thus, both solid and liquid phases will generally be involved in the real process, with a moving phase interface between them. This has been avoided in the analyses done thus far by imagining that there is only a single dense phase, a liquid. The heat of fusion for aluminum is small compared to the heat of vaporization. It has also been assumed that the thermal properties are constant. This is decidedly not true as seen from Figure 1. The approximations just noted represent considerable simplications; however, it can be expected that the general trends will be representative. Heat transfer into the dense phase is modeled by the linear heat conduction equation:

$$\rho_\ell c_\ell \frac{\partial T}{\partial t} = k_\ell \frac{\partial^2 T}{\partial x^2} \tag{1}$$

where ρ_ℓ is the liquid density, c_ℓ is its specific heat, and k_ℓ is its thermal conductivity. The possibility of convection in the liquid (driven by vapor recoil, surface tension, etc.[11]) will be neglected.

---

11. Palmer, H., "The Hydrodynamic Stability of Rapidly Evaporating Liquids at Reduced Pressure," J. Fluid Mechanics 75, 487 (1976).
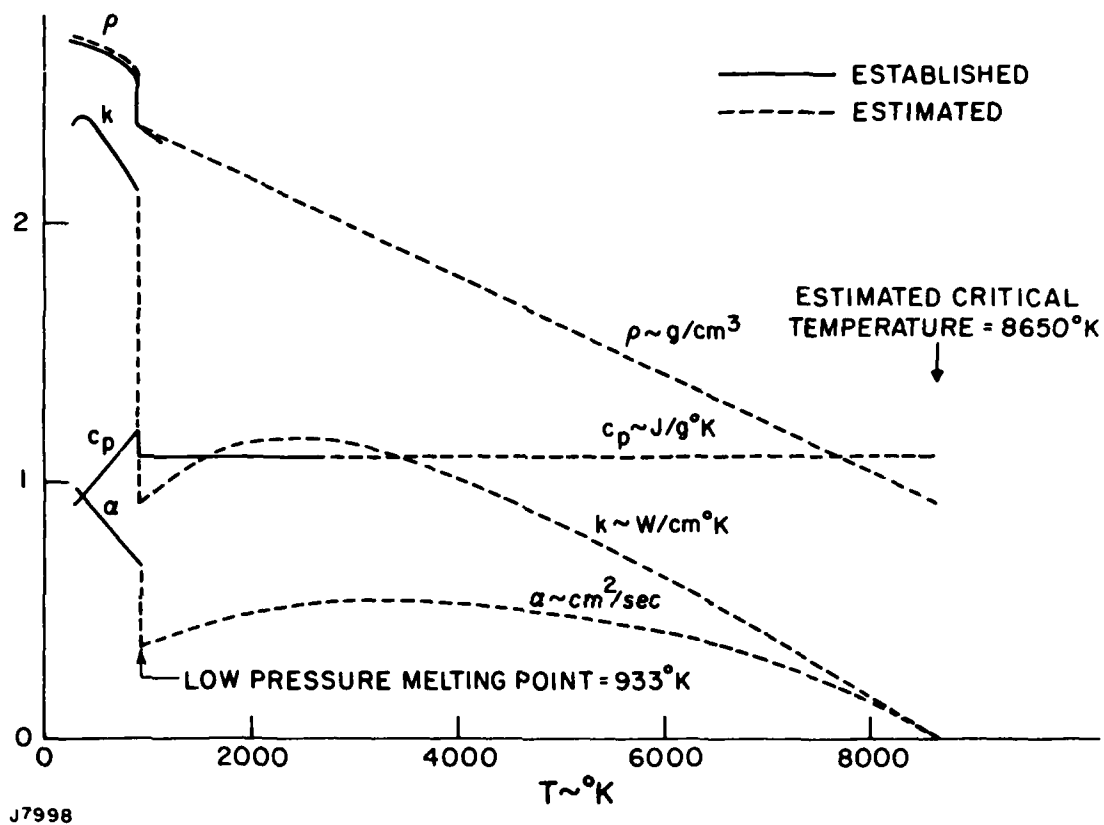
Figure 1   Properties of Pure Aluminum

The surface will recede as the aluminum boils off. This is depicted in the x-t diagram in Figure 2, where the dense phase zone lies to the left and vapor flows in the positive x-direction. It is convenient to employ a moving reference frame attached to the surface as this simplifies imposing the liquid/vapor phase jump conditions. To this end introduce $\eta = -[x + x_s(t)]$ with $x = -x_s(t)$ at the surface. The heat conduction equation becomes

$$\frac{\partial T}{\partial t} = \dot{x}_s \frac{\partial T}{\partial \eta} + \alpha_\ell \frac{\partial^2 T}{\partial \eta^2} \tag{2}$$

where $\alpha_\ell = k_\ell / \rho_\ell c_\ell$ is the thermal diffusivity and $\dot{x}_s = dx_s/dt$. Initially $T = T_i$ for all $\eta > 0$ and also this provides the appropriate boundary data as $\eta \to \infty$ for all $t > 0$.

Rapid surface vaporization can be modeled by means of Knudsen layer jump conditions.[12] These lead to the following relationships between liquid surface properties (denoted by subscript s) and vapor properties at the outer edge of the Knudsen layer where equilibrium is restored.

$$\frac{T}{T_s} = \left[\sqrt{1 + \pi \left(\frac{\gamma-1}{\gamma+1} \frac{m}{2} \right)^2} - \sqrt{\pi} \frac{\gamma+1}{\gamma-1} \frac{m}{2} \right]^2$$

$$\frac{\rho}{\rho_s} = \sqrt{\frac{T_s}{T}} \left[\left(m^2 + \frac{1}{2} \right) e^{m^2} \mathrm{erfc}(m) - \frac{m}{\sqrt{\pi}} \right] + \frac{1}{2} \frac{T_s}{T} \left[1 - \sqrt{\pi}\, m e^{m^2} \mathrm{erfc}(m) \right]$$

$$\rho u / \rho_s \sqrt{\frac{RT_s}{2\pi}} = 1 - \left(2m^2 + 1 - m\sqrt{\frac{\pi T_s}{T}} \right) \left[1 - \sqrt{\pi}\, m e^{m^2} \mathrm{erfc}(m) \right] \tag{3}$$

where γ is the ratio of specific heats, $m = u/\sqrt{2RT} = M\sqrt{\gamma/2}$, and

12. Knight, C., "Theoretical Modeling of Rapid Surface Vaporization with Back-Pressure," AIAA J. 17, 519 (1979).

16
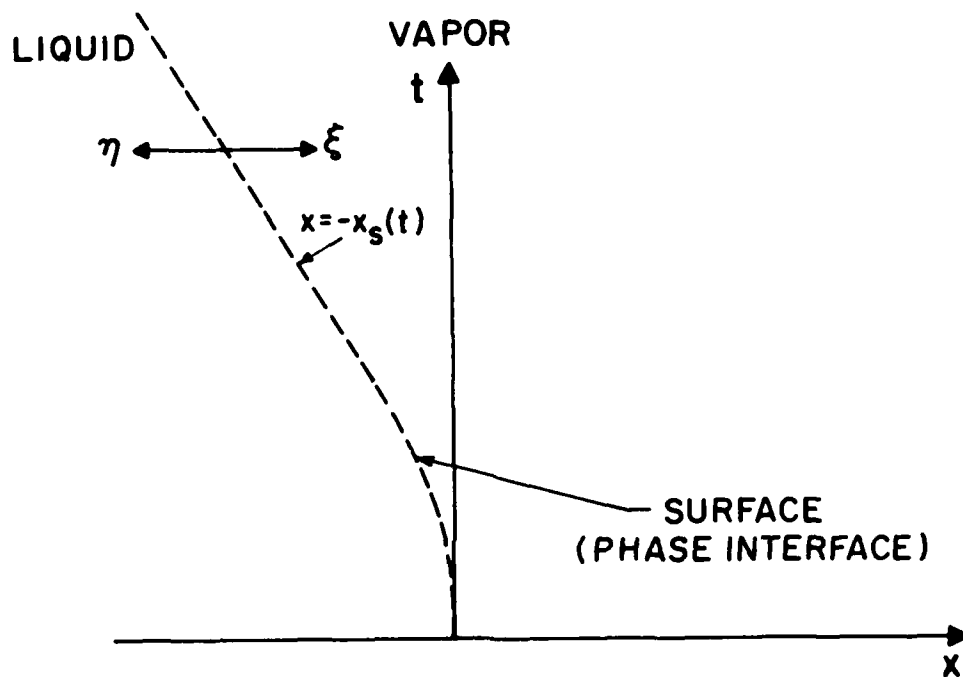
Figure 2   x-t Diagram in Lab Reference Frame

J7994

M is the flow Mach number at the outer edge of the Knudsen layer at the surface. Thermodynamic equilibrium in the liquid will be assumed so that p_s is plausibly interpreted at the saturated vapor pressure corresponding to temperature T_s. Also $\rho_s = p_s/RT_s$ since the vapor will be treated as a perfect gas. Evaluations of (3) as a function of M are given in Table 1.

A Clausius-Clayperon relation will be adopted to relate saturated vapor pressure and temperature.

$$p_s = p_b \exp\left[\frac{L_v}{RT_b}\left(1 - \frac{T_b}{T_s}\right)\right] \tag{4}$$

where $p_b = 1$ atm, T_b is the normal boiling temperature, and L_v is the (constant) heat of vaporization. For aluminum, $\gamma = 5/3$, $T_b = 2730°K$, and $L_v = 11kJ/g$ are reasonable choices. The Knudsen layer model embodied in (3) leads to a vapor stagnation temperature which is always less than T_s, implying an energy flux into the liquid. However, the temperature jump is small (<10%) and can be overlooked. Thus, energy balance at the surface is taken to be expressed by

$$\left(- k_\ell \frac{\partial T}{\partial \eta}\right)_o + \rho u L = \dot{q}_a \tag{5}$$

The __absorbed__ power per unit surface area, $\dot{q}_a$, is divided between heat conduction into the liquid and latent heat carried away by the vapor. To close the problem, mass conservation requires

$$\rho_\ell \dot{x}_s = \rho u \tag{6}$$

TABLE 1. FLOW PROPERTY RATIOS ACROSS KNUDSEN LAYER FOR $\gamma=5/3$

M	ρ/ρ_s	T/T_s	p/p_s	$\rho u/\rho_s \sqrt{\dfrac{RT_s}{2\pi}}$
0	1	1	1	0
0.05	0.927	0.980	0.908	0.148
0.1	0.861	0.960	0.827	0.273
0.2	0.748	0.922	0.690	0.465
0.4	0.576	0.851	0.490	0.688
0.6	0.457	0.785	0.358	0.786
0.8	0.371	0.725	0.269	0.817
1.0	0.308	0.669	0.206	0.816

TABLE 2. STEADY-STATE RESULTS FOR $M=1$

$\dot{Q} \sim MW/cm^2$	$T_s \sim {}^\circ K$	$p_s \sim atm$
0.1	2890	2.07
1	3570	21.8
10	4670	230
100	6750	2420
1000	11,980	24,400

19

Results are best presented in terms of nondimensional variables. To this end, let τ_p be the duration of the pulse giving rise to $\dot{q}_a$ and define $\tilde{t} = t/\tau_p$, $\tilde{\eta} = \eta/\sqrt{\alpha_\ell \tau_p}$, $\tilde{x}_s = \dot{x}_s\sqrt{\tau_p/\alpha_\ell}$, $\tilde{T} = T/T_r$, $\tilde{u} = u/a_r$, $\tilde{p} = p/p_r$, and $\tilde{\rho} = \rho/\rho_r$. Natural choices for the reference parameters are $T_r = T_b \sim 2730°K$, $a_r = \sqrt{\gamma R T_b} \sim 1.2 \times 10^5 cm/sec$, $p_r = p_b = 1$ atm, and $\rho_r = p_b/RT_b \sim 1.2 \times 10^{-4} g/cm^3$. This leads to six basic nondimensional parameters: T_i/T_b, γ, L_v/RT_b, $L_v/c_\ell T_b$, $\dot{Q}\sqrt{\alpha\ell\tau_p}/k_\ell T_b$, and $\rho_r a_r/\rho_\ell\sqrt{\tau_p/\alpha\ell}$ where $\dot{Q}$ is a characteristic <u>absorbed</u> power flux. Only the case of a top-hat absorbed power flux has been considered thus far--

$$\dot{q}_a = \begin{cases} \dot{Q} & , \quad 0 < t < \tau_p \\ 0 & , \quad t > \tau_p \end{cases} \tag{7}$$

Representative values of the thermal properties for liquid aluminum are $\rho_\ell \sim 1.6 g/cm^3$, $c_\ell \sim 1.1 J/g°K$, $k_\ell \sim 0.80 W/cm°K$, and $\alpha_\ell \sim 0.45 cm^2/sec$. Also, $T_i \sim 300°K$ is an interesting initial condition. These were used in evaluating the nondimensional parameters for what follows.

In general the problem defined above is coupled to the exterior vapor flow through the Mach number at the outer edge of the Knudsen layer, M. However, the processes are decoupled so long as the Knudsen layer remains choked (i.e., M = 1). This special case will be examined before going on to the fully coupled case. As will be seen later, the Knudsen layer remains choked only during a top-hat pulse and not afterwards. Results for

20

this special case were generated numerically for $\tau_p = 1$ μsec and are shown in Figure 3. It was necessary to use an implicit differencing procedure for an economical treatment. Note that the surface temperature approaches an asymptote during the pulse for $\dot{Q} > 10$ MW/cm^2. That steady state is defined by a balance between the vapor efflux and diffusion terms on the right side of Eq. (2). Note also that this steady state is reached increasingly rapidly as $\dot{Q}$ increases. The heat up (or cool down) time scales inversely as $\dot{Q}^2$, as might be expected from the fact that $\dot{Q}\sqrt{\tau_p}$ enters one of the nondimensional parameters above.

A straightforward analysis leads to the following steady-state distribution of temperature in the liquid.

$$T = T_i = (T_s - T_i) \exp(-\dot{x}_x \eta / \alpha_\ell) \tag{8}$$

Mass and energy balance at the surface then leads to

$$[c_\ell (T_s - T_i) + L_v] \frac{\phi p_s}{\sqrt{2\pi R T_s}} = \dot{Q} \tag{9}$$

for a time invariant absorbed power $\dot{Q}$, where $\phi = 0.816$ is the normalized mass flux for choked conditions. (Cf. Table 1) This nonlinear algebraic equation has been solved numerically to generate the results in Table 2. Note that the saturated vapor pressure at steady state increases essentially linearly with $\dot{Q}$ whereas T_s increases logarithmically. The steady-state surface temperature is well above critical conditions
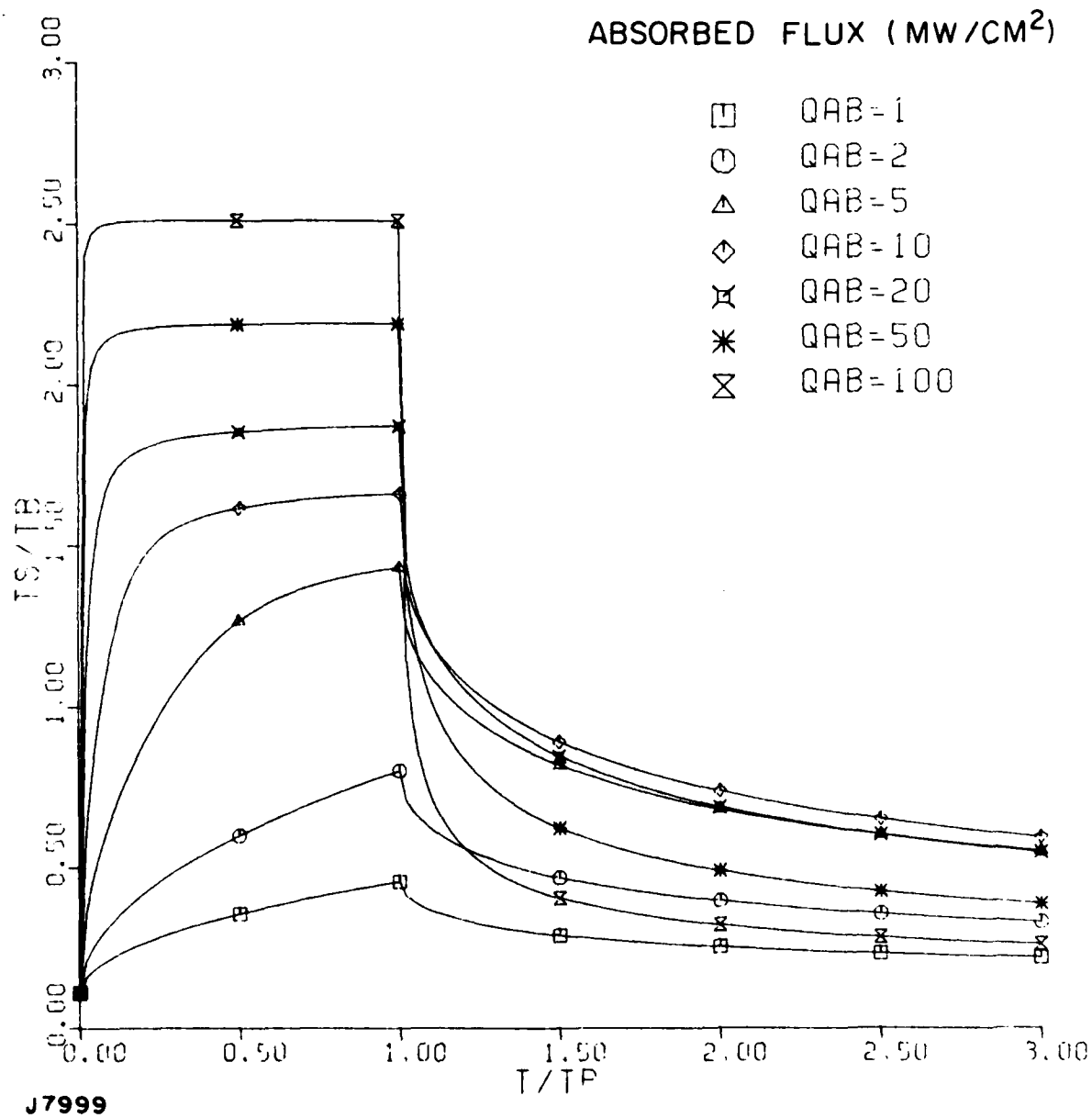
21

Figure 3   Conduction Solutions for Various Heating
             Rates, Top-Hat Input, Choked Knudsen Layer

J7999

. AVCO EVERETT

(Cf. Figure 1) for $\dot{Q}$ = 1GW/cm^2, and the predictions are highly questionable at that flux. The model predictions are meaningful for aluminum only when the absorbed power flux $\dot{q}_a \lesssim$ 100 MW/cm^2.

Turn now to the modeling for the vapor flow outside the Knudsen layer. The vapor will be treated as a nonabsorbing perfect gas, as mentioned earlier. It is again convenient to employ a moving reference plane attached to the surface. In terms of $\xi = x + x_s(t)$, the equations of motion become

$$\frac{\partial \rho}{\partial t} + \frac{\partial}{\partial \xi} (\rho u) = 0$$

$$\rho \left(\frac{\partial u}{\partial t} + u \frac{\partial u}{\partial \xi}\right) + \frac{\partial p}{\partial \xi} = \rho \ddot{x}_s \qquad (10)$$

$$\rho c_v \left(\frac{\partial T}{\partial t} + u \frac{\partial T}{\partial \xi}\right) + p \frac{\partial u}{\partial \xi} = 0$$

In the case of a top-hat energy input in Eq. (7) and a surrounding hard vacuum, no shocks will appear anywhere within the flow field. A method of characteristics then provides the best approach to solving for the exterior flow. Characteristic equations following from Eq. (10) are

$$\frac{dP}{dt} = \frac{a}{\gamma R} \frac{ds}{dt} + \ddot{x}_s \text{ on } \frac{d\xi}{dt} = u + a$$

$$\frac{dQ}{dt} = \frac{a}{\gamma R} \frac{ds}{dt} - \ddot{x}_s \text{ on } \frac{d\xi}{dt} = u - a \qquad (11)$$

$$\frac{ds}{dt} = 0 \text{ on } \frac{d\xi}{dt} = u$$

where $P = 2a/(\gamma-1) + u$ and $Q = 2a/(\gamma-1) - u$ are the Riemann invariants and s is the entropy. The directions in the first two of these equations will be referred to as P and Q characteristics, respectively.

So long as the Knudsen layer remains choked (i.e., $M = 1$), determination of surface conditions is independent of the exterior vapor flow. In that case the external flow follows by a straightforward marching procedure into $\xi > 0$, starting with known conditions at the outer edge of the Knudsen layer at $\xi = 0$. (The Knudsen layer is viewed as having infinitesimal thickness in this study.) Note that Q characteristics start with zero slope at $\xi = 0$ and that the slope will gradually become positive in $\xi > 0$. The solution domain always lies to the left of the terminal P characteristic on which $a = 0$ and u assumes an extremal value. The situation just outlined is found to persist so long as the absorbed power flux is monotonically increasing or constant in time.

If it happens that $M < 1$, as will happen when $\dot{q}_a$ decreases, the Q characteristic will have a negative slope and its origin lies outside the Knudsen layer. In that case the compatibility relation along the Q characteristic provides information determining M and hence the surface state.[12] Heat conduction, surface balance relations, and the exterior vapor flow are thereby coupled. Once the surface state is established, the rest of the exterior flow is obtained by the same sort of marching procedure noted in the previous paragraph.

24

C. RESULTS AND CONCLUSIONS

Typical evolution of surface properties are displayed in Figure 4 for $\tau_p = 1$ μsec and $\dot{Q} = 10$ MW/cm^2. Taking an absorptivity $\alpha \sim 20\%$ (as for XeF), this corresponds to an incident flux of 50 MW/cm^2, or incident fluence of 50 J/cm^2. Note that the Mach number at the outer edge of the Knudsen layer drops rapidly to zero shortly after the pulse. The possibility of $u < 0$ at the surface is disallowed because condensation has not been included in the modeling. The surface temperature after the pulse is significantly different from that in Figure 3, where $M = 1$ at all times is assumed. The saturated vapor pressure is also shown below in Figure 4. This does not directly define the force acting on the surface. Neglecting the momentum of the liquid, $\rho_\ell \, (\dot{x}_s)^2$, this is given by the momentum flux of vapor from the Knudsen layer: $F = p + \rho u^2 = p \, (1 + \gamma M^2)$. The value of F is roughly 55% of p_s for a choked Knudsen layer and can be evaluated using Table 1 more generally. Also shown in Figure 4 is the normalized mechanical impulse delivered to the surface, $\int_o^t \tilde{F} d\tilde{t}$, with $\tilde{F} = F/p_b$. Essentially all the impulse, when the surface is surrounded by vacuum, appears to be delivered during the pulse. This result will be altered if plasma effects arise, however.

Flow properties in the exterior flow at the end of the pulse ($\tilde{t} = 1$) are given in Figure 5 for $\tau_p = 1$ μsec and $\dot{Q} = 10$ MW/cm^2. Such information provides a basis for assessing whether plasma formation, due to processes such as laser-induced breakdown, is likely.

25

$$\dot{Q} = 10\,MW/cm^2,\ T_p = 1\,\mu sec$$
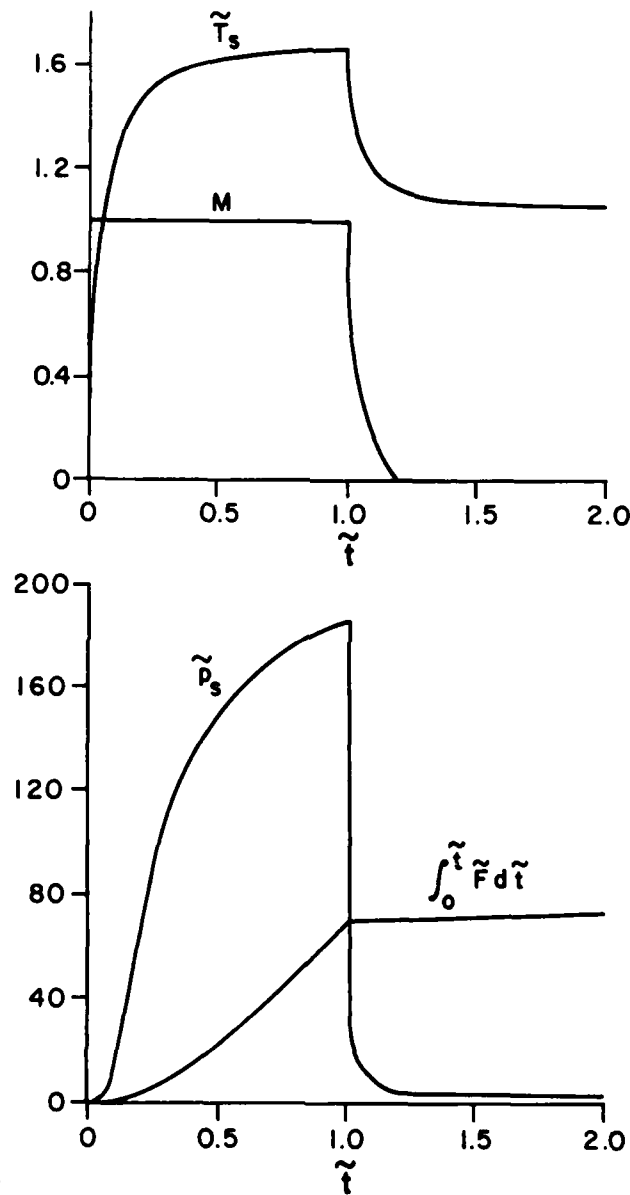
J7997

Figure 4   Evolution of Surface Properties at an Absorbed
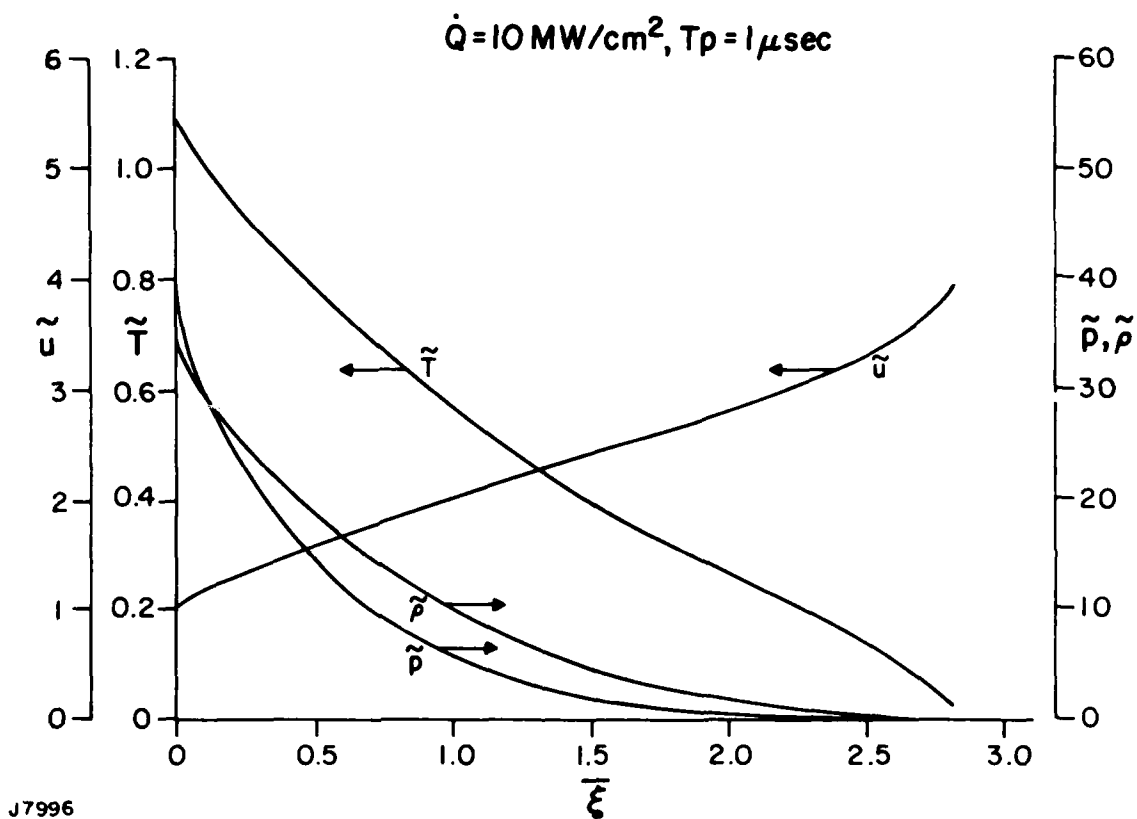Flux of 10 MW/cm^2 and a Pulse Length of 1 µsec

26

AVCO EVERETT

$\dot{Q} = 10 \, MW/cm^2, \, Tp = 1 \, \mu sec$

Figure 5   Properties in Exterior Flow at the End of a
1 μsec Pulse for an <u>Absorbed</u> Flux of 10 MW/cm²

J7996

An impulse coupling coefficient C is one parameter relevant to understanding damage mechanisms associated with pulsed devices interacting with a surface. This is normally defined in terms of the incident power density, $\dot{q}_i$, but here it will be given in terms of $\dot{q}_a$ which is typically a fraction of $\dot{q}_i$. Thus the definition used here is C_a

$$C_a = \int_0^\infty \dot{F}dt / \dot{Q}\tau_p = \frac{p_b}{\dot{Q}} \int_0^\infty \tilde{F}d\tilde{t}$$

for a top-hat input. Values for several conditions are shown in Table 3. The coupling coefficient C_a for the example in Figures 4 and 5 is ~7 taps/J of absorbed fluence, or ~1.4 based on incident fluence for $\alpha \sim 20\%$. The value of C_a is ~16 at at 100 MW/cm^2 absorbed and 1 μsec, or $C \sim 3$ for $\alpha \sim 20\%$ (XeF) and $C \sim 6$ for $\alpha \sim 40\%$ (KrF) at an incident fluence of 500 J/cm^2 and 250 J/cm^2, respectively.

In summary then, a theoretical model has been constructed in which two of the primary mechanisms influencing pulsed vaporization of an aluminum surface into surrounding vacuum are included. Moreover, the results are useful in assessing a third possible process: absorption and transfer of energy in the vapor phase. A summary of the conclusions follows:

1) Generally, heat conduction and vapor efflux represent equally important mechanisms for removing absorbed power from the surface or vapor interface.

TABLE 3. VALUES OF IMPULSE COUPLING COEFFICIENT DURING THE PULSE,

$$C_a = \frac{p_b}{\dot{q}_a} \int_o^1 F\, dt \quad \text{dyne-sec/J}$$

$\dot{q}_a$ \ τ_p	1μsec	2μsec	4μsec
10 MW/cm^2	7.03	9.18	10.81
30 MW/cm^2	12.25	13.30	14.15
100 MW/cm^2	15.90	16.90	---

2) The surface heat-up time varies inversely with the square of the absorbed power and can become small compared to the incident pulse duration at absorbed fluxes >20 MW/cm^2, or, for the XeF absorptivity of 20%, at incident XeF fluxes >100 MW/cm^2.

3) The Knudsen layer attached to the surface tends to be choked when the absorbed power is increasing and unchoked when the power is decreasing. The problem is fully coupled when the Knudsen layer is unchoked.

A fully coupled theoretical analysis of the sort pursued in this Section is new and has not been published before for the case of transient vaporization into vacuum.

III.   PLASMA FORMATION IN ALUMINUM VAPOR

A.   INTRODUCTION

In the previous section, an analysis was presented that predicts aluminum vapor conditions under irradiation by a high-power UV laser.   Under these conditions, it is possible for a plasma to form.   It is the objective of this section to determine the flux level for plasma onset at the XeF wavelength (353 nm).

B.   MODEL

In order to develop a tractable model for plasma formation in aluminum vapor irradiated by an XeF laser, simplifying assumptions must be made about the electronic structure of aluminum. We use the energy level diagram of aluminum shown in Figure 6 as the starting point for our approximations.   This figure shows all of the excited states up to 4.7 eV above the ground state and the first ionization limit at 5.98 eV.   The first excited state is 3.14 eV above the ground state and is optically accessible from the ground state and, thus, is expected to be important in energy storage in aluminum vapor.   The second excited state is a $(3s3p)^2$ ^4P state.   Since optical transition to this state from the ground state is both spin and angular momentum forbidden, its influence on energy storage in the vapor is probably negligible and, thus, has been omitted from our model.   Immediately

31
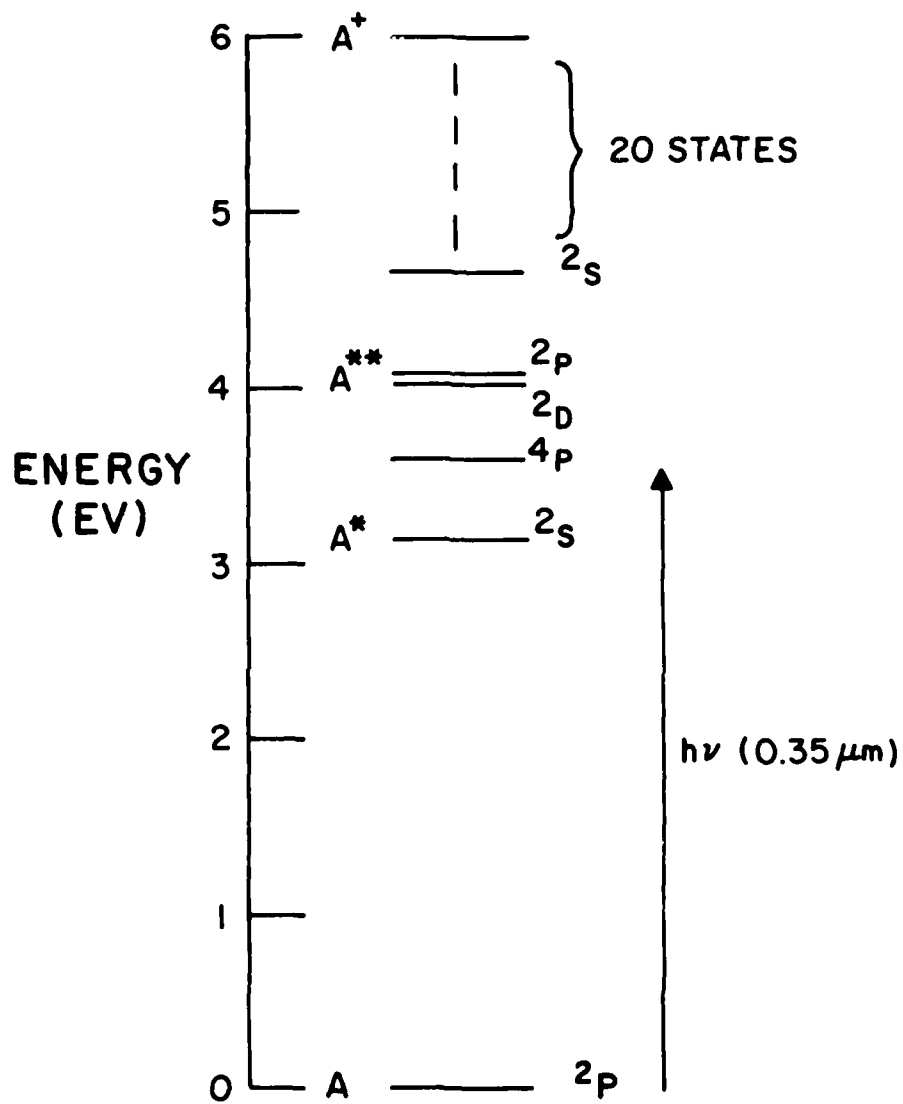
Figure 6   Energy Level Diagram for Aluminum

J7995

above the ^4P state are the $(3s^23d)^2D$ and $(3s^24p)^2P$ states which lie within kT of each other for all temperatures of interest for our application. The next excited state, a ^2S state, occurs at 4.67 eV and at higher energies, excited states are plentiful up to the first ionization limit.

For our calculations, we have assumed that the electronic manifold of staes in aluminum can be represented by the ground state, Al, two excited states, Al* and Al**, and a singly ionized state, Al$^+$. One excited state, Al*, corresponds to the first excited state, $(3s^24s)^2S$ of aluminum. Excitation to this state is expected to be the rate limiting step for ionization, since this process requires the transfer of 3.1 eV of energy and only 2.9 eV are required to complete the ionization. The other excited state, Al**, represents a combination of the $(3s^23d)^2P$ states. This state can be easily formed by transitions from both the ground and first excited states. Once the Al** state is formed, excitation, and subsequent ionization, is expected to occur rapidly due to the density of states between the Al** state and the ionization limit, therefore, including more highly excited states in our model is not considered necessary. Only the singly charged ion is included in our model since the multiply ionized states do not become important until temperatures of a few eV are reached.

In our model, excitation of aluminum vapor is assumed to occur by two mechanisms; electron impact excitation and photo-ionization. These processes can be represented by the following reactions:

33

Electron impact excitation and ionization:

$$Al + e \rightarrow Al^* + e \qquad (1)$$

$$Al + e \rightarrow Al^{**} + e \qquad (2)$$

$$Al^* + e \rightarrow Al^{**} + e \qquad (3)$$

$$Al^{**} + e \rightarrow Al^+ + 2e \qquad (4)$$

Photoionization

$$Al^* + h\nu \rightarrow Al+ + e \qquad (5)$$

$$Al^{**} + h\nu \rightarrow Al^+ + e \qquad (6)$$

Direct electron impact ionization of the Al and Al* states is not included in our model since it would be much slower than the competing process of excitation to Al** and subsequent ionization from that state.

Other processes which may affect the electron temperature and, hence, the rate of vapor heating are momentum transfer from the electrons to the heavy particles (reaction (7)) and inverse Bremsstrahlung absorption of the laser radiation by electrons in the presence of neutral or ionic aluminum.

Also necessary for our modeling of plasma formation in aluminum vapor are rate constants for the reactions listed above. A first cut at the electron impact excitation rate constants for reactions (1)-(3) can be made by using the following expression:[13]

$$k_{ij} = 1.58 \times 10^{-5} \ \frac{f}{\sqrt{T_e} \ W_e} \ e^{-W_e/kT_e} \ P\!\left(\frac{W_e}{kT_e}\right) \quad (cm^3/sec)$$

where f is the optical oscillator strength of the transition $i \rightarrow j$, W_e is the energy of the transition, T_e is the electron temperature

34

and $P(x)$ is a tabulated function.[13] The rate constant for the reverse reaction can be obtained by detailed balancing.

$$k_{ji} = \frac{g_i}{g_j} k_{ij} \, e^{W_e/kT_e}$$

where g_i and g_j are the degeneracies of the lower and upper states, respectively.

A reasonable rate constant for the remaining electron impact process, $Al^{**} + e \rightarrow Al^+ + 2e$, (reaction (4)) is more difficult to determine. While a rate constant for direct ionization from the Al^{**} state can be calculated,[13] this constant will be a lower bound on the true value since ionization of the Al^{**} state can also occur via multistep excitation followed by ionization from a highly excited electronic state whose rate constant for ionization will be much larger than that for the Al^{**} state. This multistep process will increase the effective rate for ionization and, indeed, will probably be the dominant ionization channel. In our model, we have therefore assumed that the lifetime for ionization from the Al^{**} state is approximately three times longer than the lifetime for excitation to the next more energetic level, since three transtions of this energy separation are just sufficient for ionization. The rate constant obtained using this approximation is appreciably larger than that for direct ionization.

13. Allen, C.W., Astrophysical Quantities, 2nd Edition, Athlone Press, London, 1963, p. 42.

As will be seen from our computer results, the time necessary for plasma formation is sensitive to the rate constant for the reverse of reaction (4). Therefore, a more accurate method of estimating this rate constant would be desirable and would increase the reliability of our computer predictions.

The expression given above for the electron impact excitation rate constants was derived using a Maxwellian energy distribution for the electrons. For appreciable excited state densities which can occur in the regime of interest for this study, this approximation breaks down and a more accurate method of calculating rate constants which allows for a non-Maxwellian distribution should be considered in future work.

Cross sections for photoionization from the $4s^2S$, $3d^2D$ and $4p^2P$ states which appear in our model (reactions (5) and (6)) can be calculated using the quantum defect method of Burgess and Seaton.[14] The cross section for ionization from the 4s state possesses a Cooper minimum. This phenomenon has also be observed for ionization from s states in the alkalis[15] and rare gases.[16] The cross section for ionization by an XeF photon will occur near this Cooper minimum, thus causing that process to have an anonalously small cross section. No such minimum occurs in the 3d cross section and while a minimum does occur in the $4p \rightarrow 3d$ cross

14. Burgess, A. and Seaton, M.J., Mon. Notices Roy. Astron. Soc. 120, 121 (1960).

15. Fano, U., Cooper, J.W., Rev. Mod. Phys. 40, 441 (1968).

16. Duzy, C. and Hyman, H.A., Phys. Rev. A. 22, 1878, (1980).

section, ionization by an XeF photon is not near this dip in the
cross section. For absorption of 353 nm photons the cross sec-
tions for the 4s, 3d, 4p states are 4.9×10^{-19} cm^2, 1.1×10^{-17} cm^2,
and 7.0×10^{-18} cm^2, respectively. In our model, the Al* state has
a photoionization cross section of 4.9×10^{-19} cm^2 while that for
the Al** state is 9.4×10^{-18} cm^2. This difference in behavior
of the 4s state toward the incident radiation is the main reason
for our choosing to include two excited states in our model.
This approach differs from that used by Rosen, et al.[5]

Of the remaining processes mentioned previously and included
in our model, neutral inverse Bremsstrahlung (reaction (9) in
our code) is expected to have the greatest effect on plasma form-
ation. All calculations of the cross section for this process
to date have been based on the assumption that absorption of a
photon by an electron causes only a negligible change in the
momentum of the electron.[7] This assumption is obviously not
valid when absorption of a 3.5 eV XeF photon is being considered.
However, until a more appropriate estimate is available, we will
use the existing expression[17]

$$\sigma = 1.88 \times 10^{-15} \sqrt{\alpha} \ \lambda^3 T_e \ (cm^5)$$

where α is the polarizability of the atom in cm^3, λ is the wave-
length of the absorbed radiation in cm and T_e is the mean electron
temperature in eV.

---

17. Hyman, H.A., Kivel, B. and Bethe, H.A., AERL Report #AMP
    377, April 1973.

Inverse Bremsstrahlung absorption in the presence of an atomic ion (reaction (8)) has the following cross section:[18]

$$\sigma = 1.25 \times 10^{-25} \; \lambda^3 / \sqrt{T_e} \;\; (cm^5)$$

where λ and T_e are as defined above.

The reactions described above and their rate constants or cross sections were incorporated into a computer code and the time evolution of the system was followed. The starting densities of the various species were obtained from the calculation of vapor pressure and temperature described in Section II. Since the plasma code assumes constant vapor density, we chose as initial conditions values just outside the Knudsen layer, at a time of 1/2 the pulse length. As will be shown below, the choice of this particular time within the pulse is not important because plasma breakdown occurs at fluxes high enough that the vapor reaches steady state early in the pulse.

C. RESULTS

We will now present numerical results from the computer model described avove. The initial conditions for our computer model were obtained as described previously using the results of Section II. In Table 4, the heavy particle density and the heavy particle and electron temperatures are listed as a function of incident flux. The remaining densities can be generated using this information and the thermal equilibrium assumption. In the

18. Zel'dovich, Ya B., Raiser, Yu P., Physics of Shock Waves and High-Temperature Hydrodynamics Phenomena, Vol. 1, p. 259, Academic Press, New York, 1966.

TABLE 4. INITIAL CONDITIONS FOR PLASMA KINETICS CALCULATIONS

Incident flux, q_i	Absorbed flux q_a	Vapor Pressure	Vapor Temperature, T_g		Electron Temperature, T_e	
(MW/cm^2)	(MW/cm^2)	(atm)	(°K)	(eV)	(°K)	(eV)
10	2	3×10^{-5}	1100	0.094	1640	0.141
25	5	3.1	2300	0.198	3440	0.296
50	10	31	2960	0.255	4420	0.381
100	20	85	3380	0.291	5050	0.435
250	50	250	4000	0.345	5980	0.515

$T_e = T_g/0.669$

39

previous section, the results were expressed in terms of the absorbed flux, since that is the dominant parameter in that calculation. In this section the results are expressed in terms of the _incident_ flux, which is the more important parameter here. The two are related by the absorptivity α, which is taken to be 20% at the XeF wavelength. Beginning at the highest _incident_ flux density considered (250 MW/cm^2) (or 50 MW/cm^2 absorbed), we see in Figure 7 that the electron temperature rises to 1.0 eV in 0.057 µsec, at which time breakdown may be considered to have occurred due to the rapidity with which ions are formed at this temperature and the particle densities considered in this work. Above 1 eV our model with its assumed Maxwellian electron distribution, becomes increasingly unrealistic, so the calculation is stopped at T_e = 1.5 eV.

Figure 7 shows that the temperature of the heavy particles, T_g, also begins to rise rapidly after 10^{-8} sec, and momentum transfer is sufficient to equilibrate energy between electrons and atoms.

The electron density (n_e) shows a similar history, as seen in Figure 8. The concentration of excited aluminum atoms also rises rapidly during the breakdown period.

At an incident flux density of 100 MW/cm^2 the breakdown occurs more slowly than at 250 MW/cm^2. As we see in Figure 9, the electron temperature reaches 1.0 eV in 0.092 sec. Figure 10 shows an avalanche of ionization and atomic excitation, also delayed relative to the 250 MW/cm^2 case.
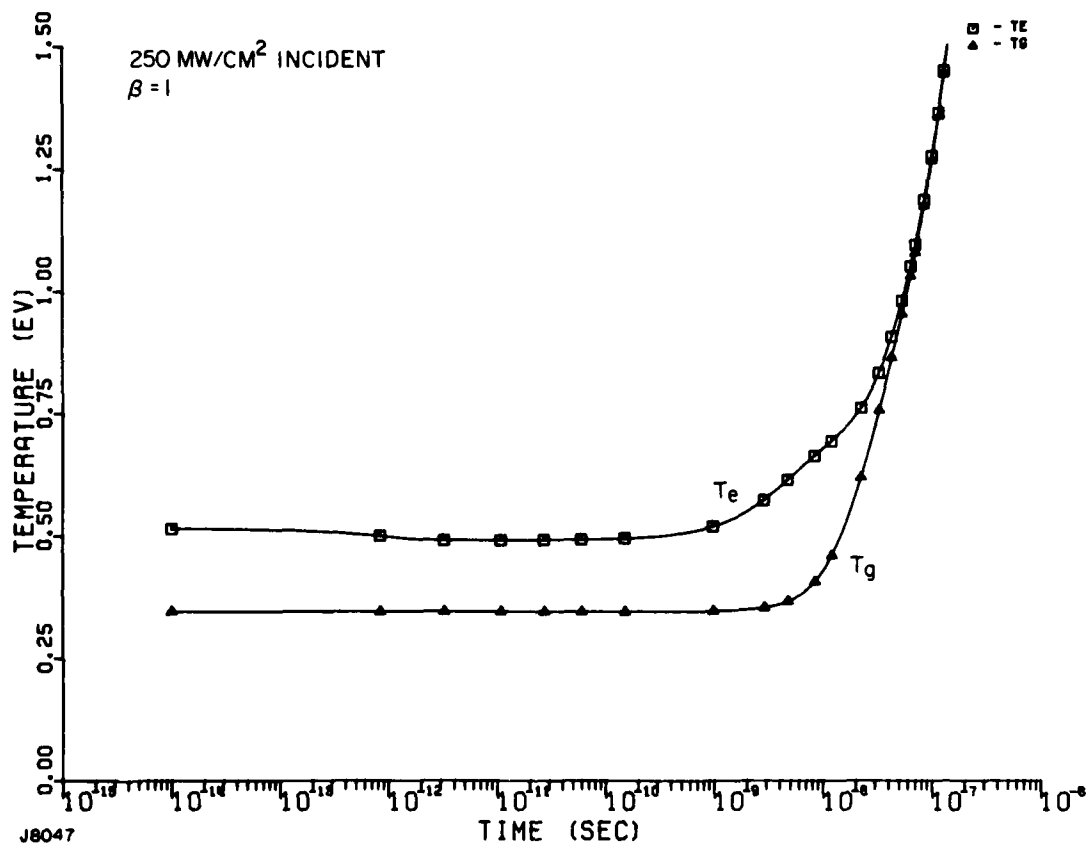
40

Figure 7   Temperature of Electrons (T_e) and Temperature of
            Aluminum Atoms and Ions (T_g) for an Incident Flux
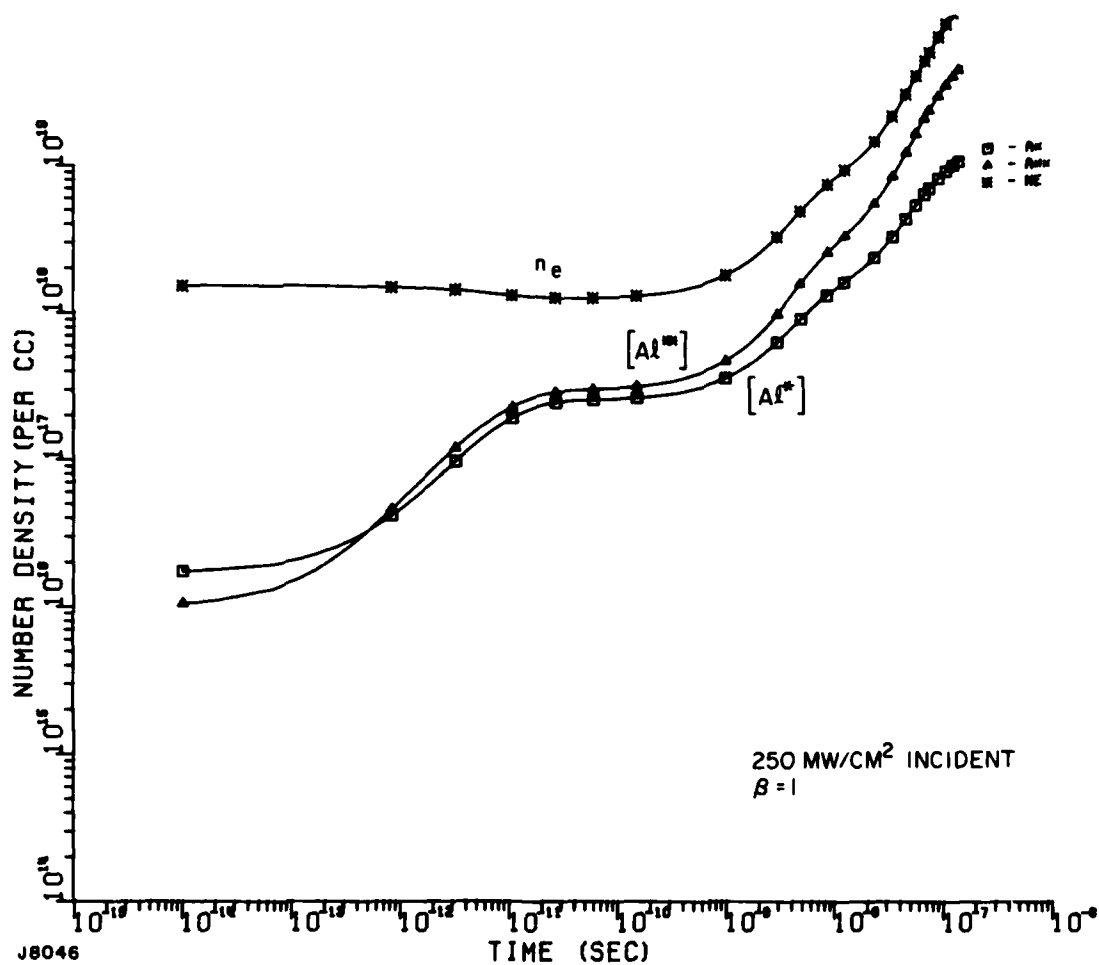   Density of 250 MW/cm^2

41

Figure 8   Concentration of Electrons (n_e) and Excited Aluminum
             Atoms ([Aℓ*] and [Aℓ**]) at 250 MW/cm^2
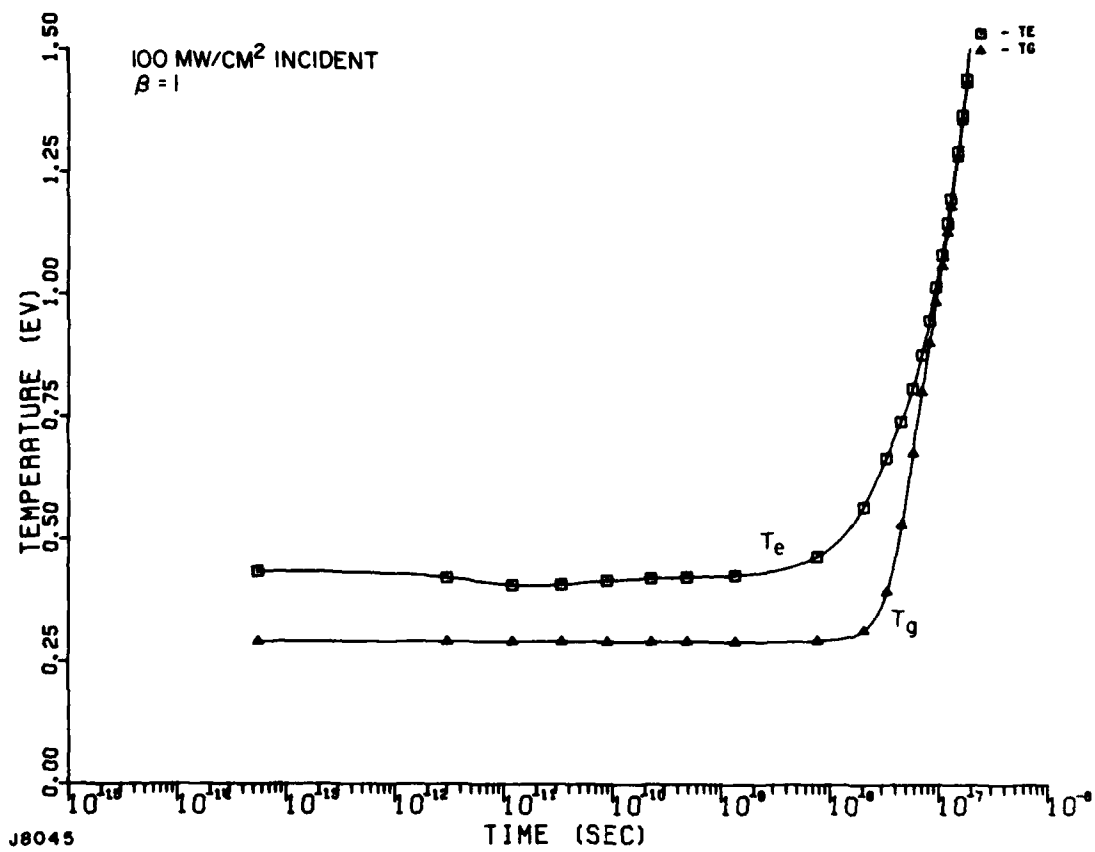
Figure 9   Electron and Gas Temperatures at 100 MW/cm^2
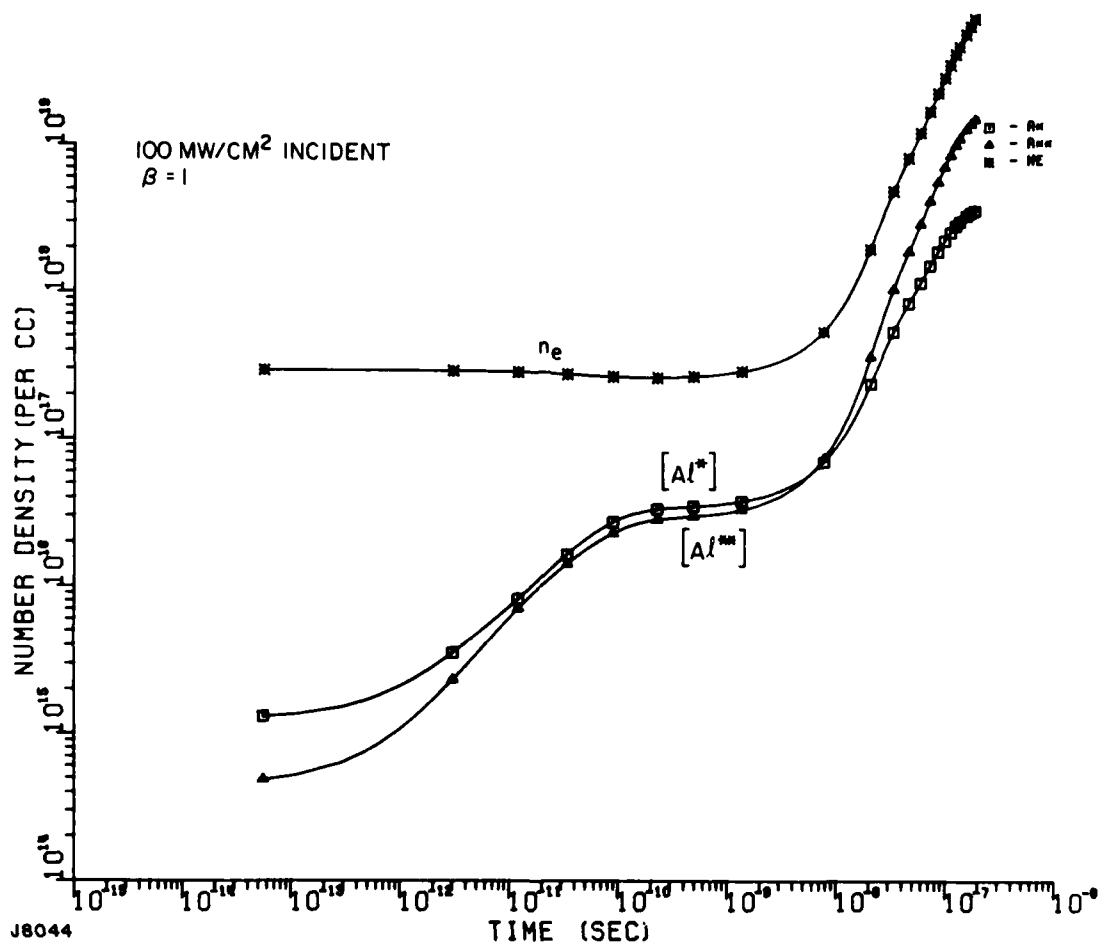
Figure 10   Electron and Excited Atom Densities at 100 MW/cm^2

44

Rates of individual reactions (1)-(6)(8) and (9) are plotted in Figures 11 and 12 in part/cm^3-sec for an incident flux of 100 MW/cm^2. Reactions going in the forward direction appear in Figure 11, while those going backwards are shown in Figure 12.

We observe in these figures three distinct reactions regimes. (a) During the first 10^{-10} sec the production of excited aluminum atoms dominates via the reactions

$$Al + e \rightarrow Al^* + e, \qquad (1)$$

$$Al + e \rightarrow Al^{**} + e, \qquad (2)$$

$$Al^{**} + e \leftarrow Al^+ + 2e. \qquad (4-)$$

In this regime the ion density falls slightly. This is associated with the slight decrease in electron temperature which occurs as the aluminum is excited. (b) From 2×10^{-10} to 4×10^{-9} the scene is relatively quiet. The chief reaction is

$$Al^{**} + h\nu \rightarrow Al^+ + e, \qquad (6)$$

but almost all of the ionization is neutralized by reaction (4-). Reaction (6) gradually builds up the electron concentration so that reaction (2) comes to life again. In addition to creating more electrons, reaction (6) is also the main mechanism for heating electrons. Since the Al** state is only 1.9 eV below the ionization limit, absorption of an XeF (3.5 eV) photon creates an electron with 1.6 eV of energy, which is considerably above the mean electron energy. The importance of this will be evident later. (c) After 7×10^{-9} sec, the combination of reactions (2) and (6) leads to avalanche ionization.
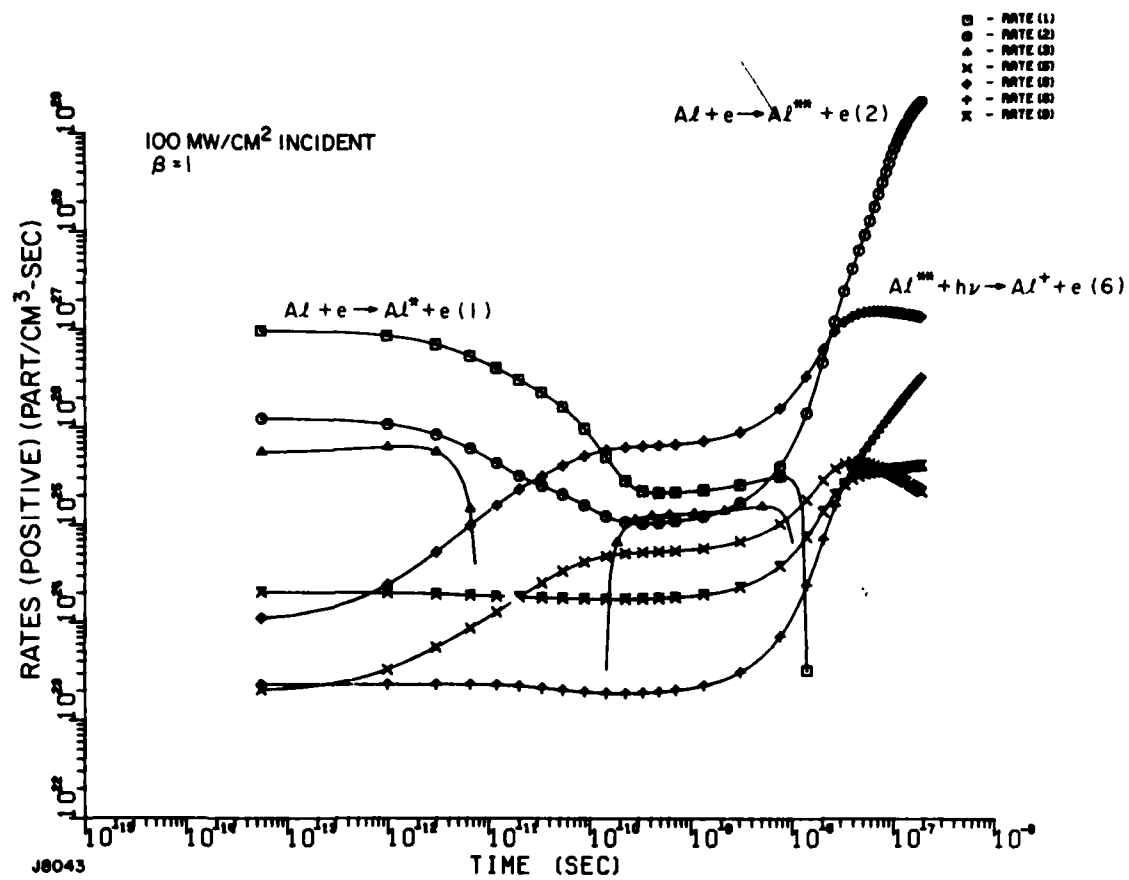
45

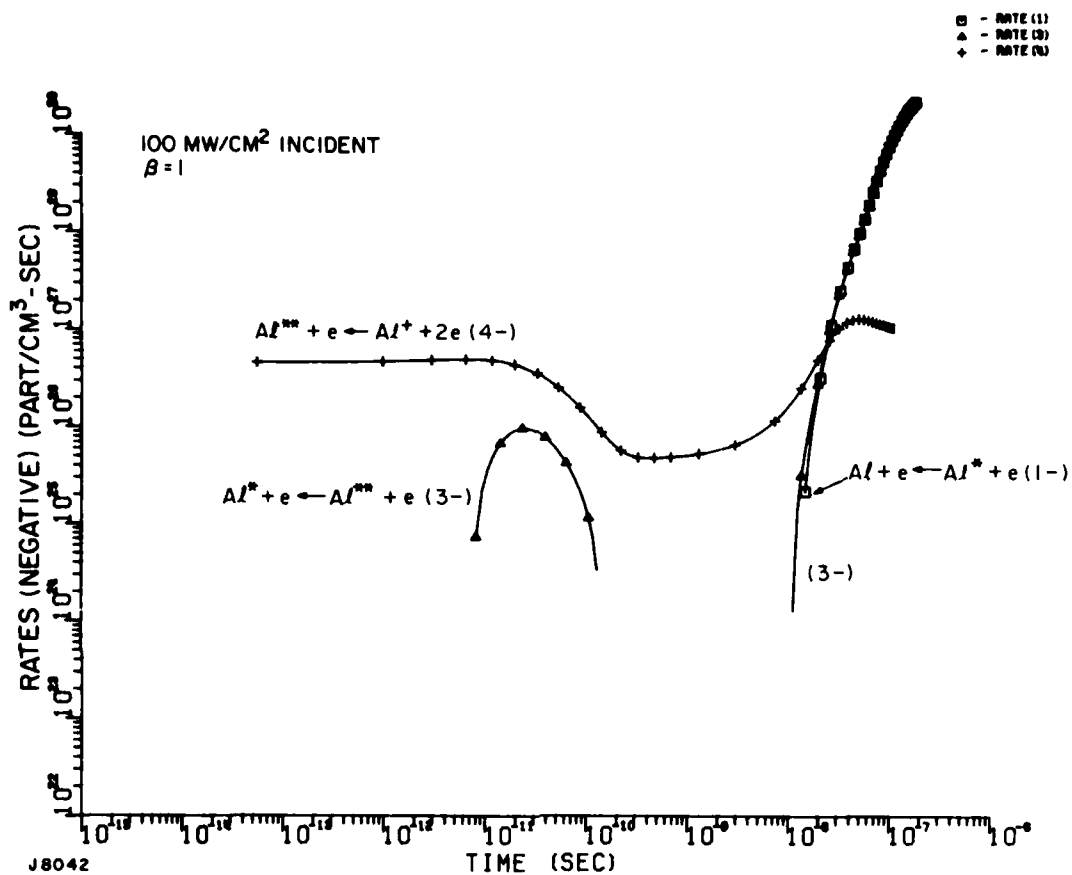Figure 11   Forward Reaction Rates at 100 MW/cm^2

Figure 12   Reverse Reaction Rates at 100 MW/cm^2

47

The breakdown mechanism is similar at 50 and 250 MW/cm^2. At an incident flux of 50 MW/cm^2 (10 MW/cm^2 absorbed) we find that breakdown is sensitive to the rate constant for the reverse of reaction (4). The above discussion of our model indicated uncertainties concerning this reaction. The recombination rate constant (4-) is obtained by multiplying the ionization rate constant by the Saha expression in which the energy W of the reaction $Al^{**} + e \rightarrow A^+ + 2e$ (4) appears in a positive exponent. Such a formalism implies a one-step process. Actually, recombination will involve several steps. To model this, we replace the energy in the exponent by W/β, with β an adjustable parameter. Thus, $\beta = 1$ corresponds to a single step for reaction (4-1), while $\beta = 3$ corresponds to three steps.

The cases presented above are for $\beta = 1$. At 50 MW/cm^2 incident, we have breakdown ($T_e \rightarrow 1.0$ eV) in 0.21 µsec if $\beta = 1$, as displayed in Figures 13 and 14. If $\beta = 2$ or 3, however, no breakdown occurs within 2 µsec (Figures 15 and 16).

Since reaction (4-) is the only mechanism for removal of electrons from the vapor, one would expect a decrease in its rate constant (i.e., increasing β) to decrease the time necessary for breakdown. Actually, the opposite occurs.

This seemingly paradoxical situation can be explained as follows. The explanation hinges on the fact that the main electron heating mechanism in our model is photoionization from the Al^{**} state. As the rate constant for recombination is increased (β decreased) more Al^{**} states are formed relative to the number
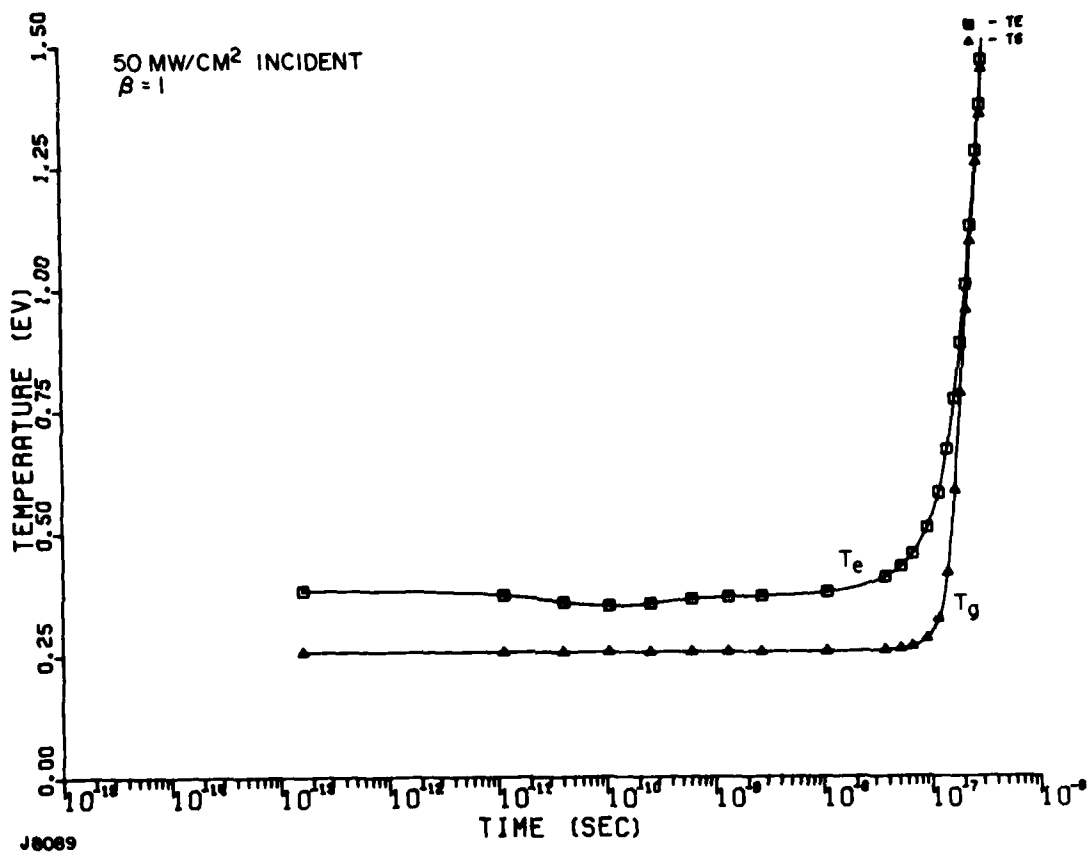
48

Figure 13   Electron and Gas Temperatures at 50 MW/cm^2
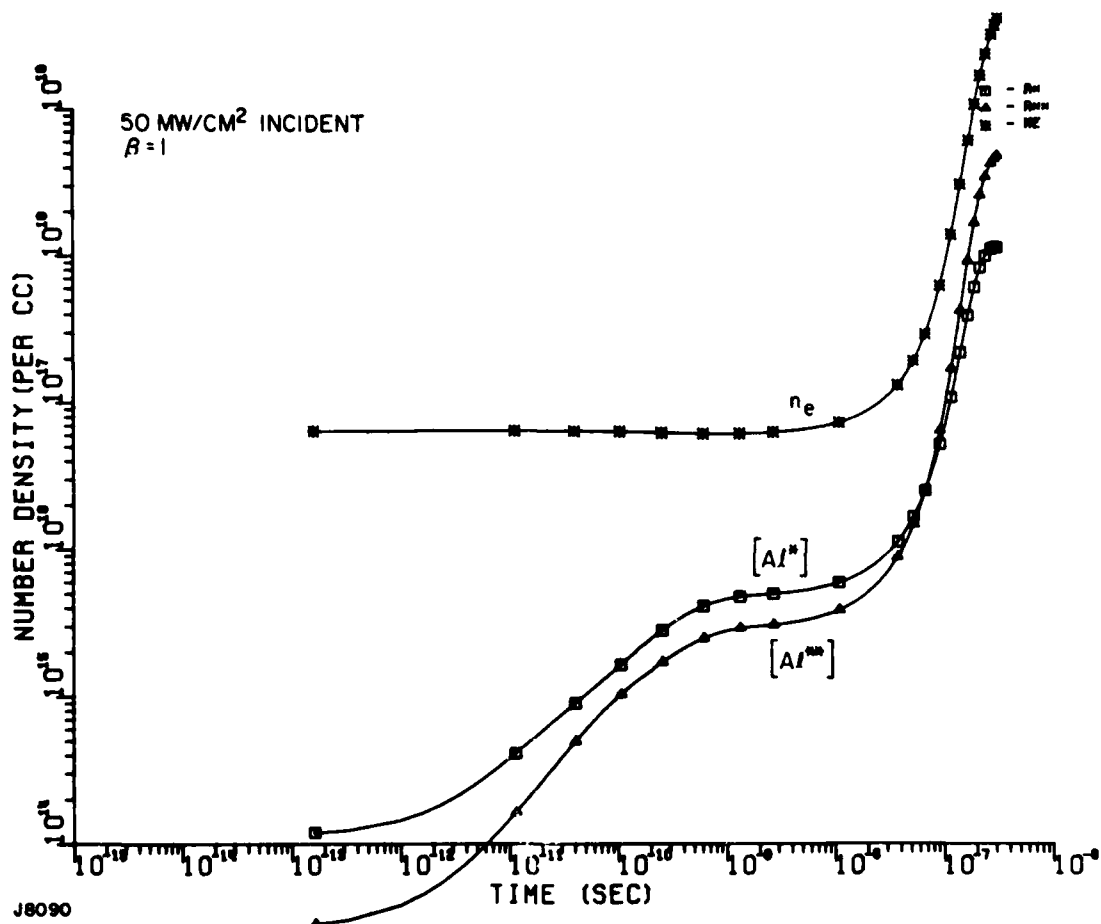
49

Figure 14   Electron and Excited Atom Densities at 50 MW/cm^2
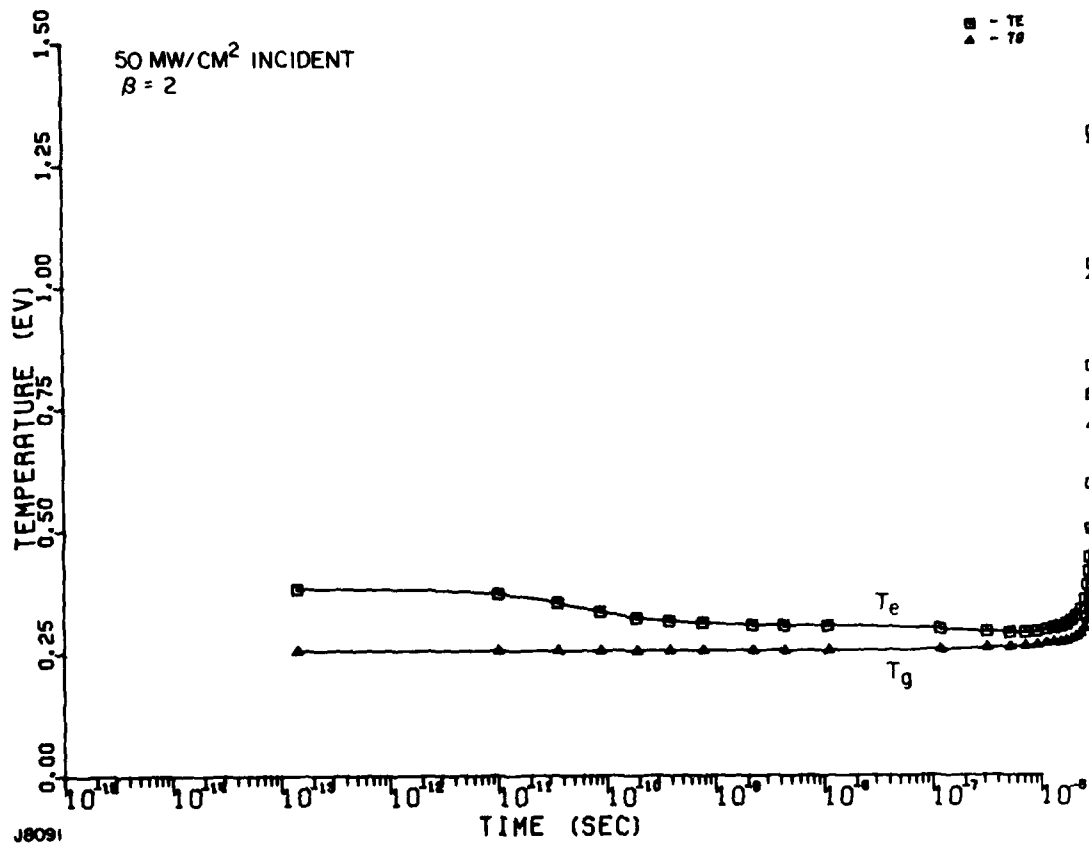
Figure 15   Electron and Gas Temperatures at 50 MW/cm^2.
Here $\beta = 2$; i.e., the rate constant for reaction
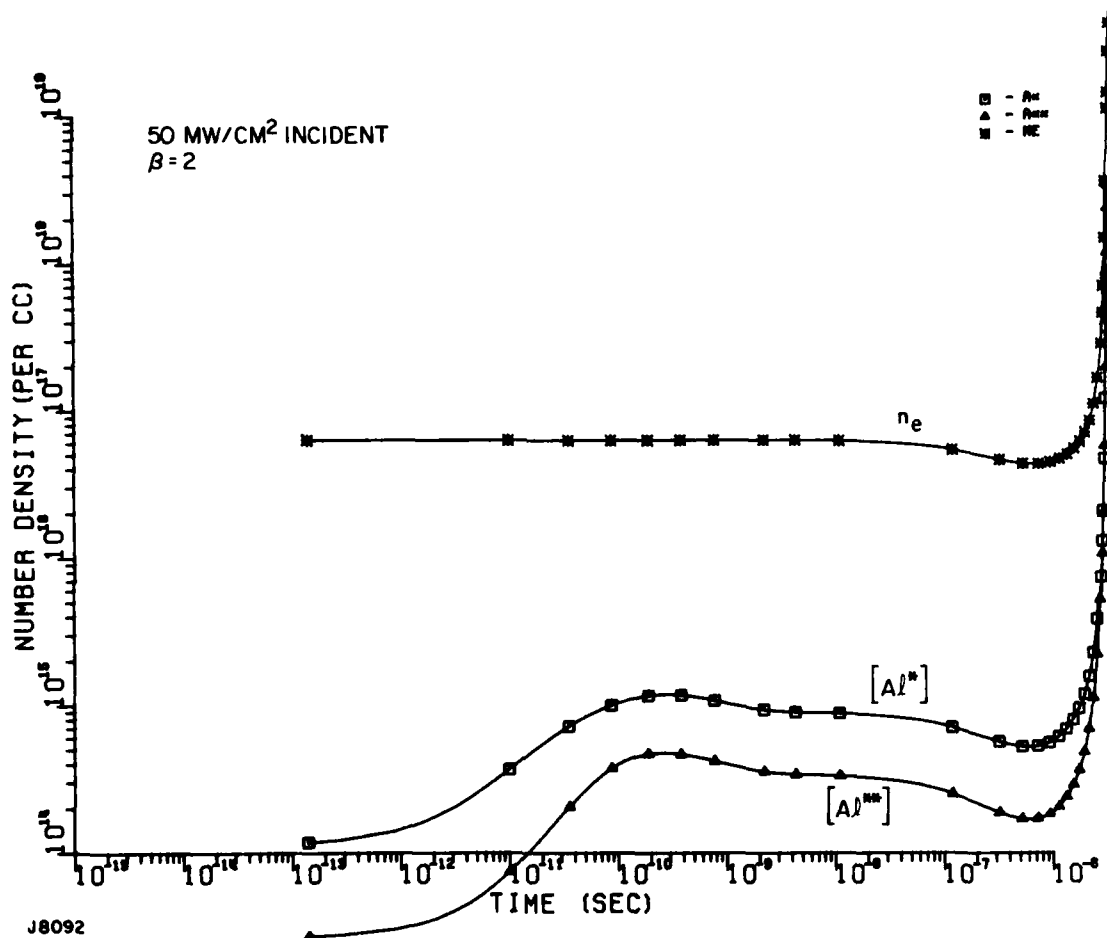(4-) is reduced. *Breakdown occurs after* 3.1 μsec.

Figure 16   Electron and Excited Atoms at 50 MW/cm^2.
Here β = 2.

of ions present. These Al** states can photoionize which pro-
duces hot electrons which in turn increase the mean electron
temperature. This higher electron temperature increases the
rate of excitated state production via electron impact, so more
Al** states are formed and the process continues. If the num-
ber of Al** states available for photoionization is decreased
by decreasing the recombination rate, the electron heating rate
will decrease and the onset of breakdown will be delayed as is
seen in our results. In other words, to achieve breakdown, it
pays to sacrifice a few electrons in order to heat up the re-
mainder.

The effect of β on the time to achieve $T_e = 1.0$ eV is
summarized in Table 5. it appears that the rate constant for
reaction (4-) has a critical effect on whether or not breakdown
occurs within a given time.

These results naturally depend upon the initial conditions.
The time to achieve breakdown evidently decreases as the initial
electron density increases.

No breakdown at all occurred at 25 MW/cm^2 incident.

D. CONCLUSIONS

Plasma formation was not predicted at 25 MW/cm^2 for any of
the sets of rate constants considered in this work while at
100 MW/cm^2 plasma was formed very rapidly regardless of the
assumptions used for determining the rate constants. For flux
levels between these two extremes our results indicate that the
relative magnitude of the photoionization and electron impact
ionization rates determine whether a plasma is present.

TABLE 5. TIME (μsec) FOR ELECTRON TEMPERATURE TO REACH 1 eV
IN ALUMINUM VAPOR PLASMA

q_{inc} MW/cm^2 $\diagdown$ β	1	2	3
10	> 2.	> 2.	
25	> 2	> 2	
50	0.21	3.1	> 2.
100	0.092	0.22	
250	0.057		

For a 0.5 μsec pulse for which data exist[4,5] our code results suggest that a plasma should not be present for fluences < 10 J/cm^2 and will almost certainly be present above 50 J/cm^2. This conclusion is consistent with the existing experimental results. Rosen, et al.[5] first observed a decrease in reflected laser intensity at ~30 J/cm^2. This value lies within the exprected range for the onset of plasma formation.

Several improvements could be made in our model which would increase its reliability and we suggest their inclusion in future work. The inclusion of a non-Maxwellian electron distribution for determining the electron impact rate constants is one such improvement. This correction could be very important when large numbers of excited atoms are present. Further thought should also be given to the expression used for estimating electron impact ionization.

Uncertainty also exists in our calculation of the cross section for photoionization from the 4p state due to the difficulty in estimating the quantum defect for the 4p→3d transition. A more detailed calculation could eliminate this ambiquity.

One effect which was not considered in our model is re-radiation by the aluminum vapor plasma. While the net energy lost by this mechanism is probably small when averaged over the entire vapor, reradiation is the mechanism by which energy is coupled from the plasma to the surface, and therefore should be studied in detail. Multiply - charged ions should also be included.

55

REFERENCES

1. McKay, J.A., Schriempf, J.T., Cronburg, T.L., Eninger, J.E., and Woodroffe, J.A., "Pulsed CO_2 Laser Interaction with a Metal Surface at Oblique Incidence," Appl. Phys. Lett. 36, 125 (1980).

2. Jacob, J.H., Hsia, J.C., Mangano, J.A., and Rokni, M., J. Appl. Phys. 50, 5130 (1979).

3. Woodroffe, J.A., Hsia, J., Ballantyne, A., "Thermal and Impulse Coupling to an Aluminum Surface by a Pulsed KrF Laser," Appl. Phys. Lett. 36, 14 (1980).

4. Duzy, C., Woodroffe, J.A., Hsia, J. and Ballantyne, A., Interaction of a Pulsed XeF Laser with an Aluminum Surface," Appl. Phys. Lett. 37, 542 (1980).

5. Rosen, D.I., Mittledorf, J., Kothandaraman, G., Pirri, A.N., and Pugh, E.R., AIAA Paper No. AIAA-80-1321, presented at 13th Fluid Plasma Dynamics Conference, Snowmass, Colorado, July 1980.

6. Walters, C.T., "Ultraviolet Laser Effects Experiments," Report #BCL-G7029, Battelle Columbus Laboratories, Columbus, Ohio (1980).

7. Reilly, J., Ballantyne, A., Woodroffe, J.A., "Modelling of Momentum Transfer to a Surface by Laser Supported Absorption Waves," AIAA J. 17, 1098 (1979).

8. Pirri, A.N., Root, R.C., and Wu, P.K.S., "Plasma Energy Transfer to Metal Surfaces Irradiated by Pulsed Lasers," AIAA J. 16, 1296 (1978).

9. Shui, V., Kivel, B., and Weyl, G., "Effect of Vapor Plasma on the Coupling of Laser Radiation with Aluminum Targets," J. Quantum Spectroscopy and Radiative Transfer 20, 627 (1978).

10. Weyl, G., Pirri, A., Root, R., "Laser Ignition of Plasma Off Aluminum Surfaces," AIAA-80-1319, 13th Fluid and Plasma Dynamics Conference, July, 1980.

11. Palmer, H. "The Hydrodynamic Stability of Rapidly Evaporating Liquids at Reduced Pressure," J. Fluid Mechanics 75, 487 (1976).

12. Knight, C., "Theoretical Modeling of Rapid Surface Vaporization with Back-Pressure," AIAA J. <u>17</u>, 519 (1979).

13. Allen, C.W., <u>Astrophysical Quantities</u>, 2nd Edition, Athlone Press, London, 1963, p.42.

14. Burgess, A. and Seaton, M.J., Mon. Notices Roy. Astron. Soc. <u>120</u>, 121 (1960).

15. Fano, U. and Cooper, J.W., Rev. Mod. Phys. <u>40</u>, 441 (1968).

16. Duzy, C. and Hyman, H.A., Phys. Rev. A. <u>22</u>, 1878, (1980).

17. Hyman, H.A., Kivel, B. and Bethe, H.A., AERL Report AMP #377, April 1973.

18. Zel'dovich, Ya B. and Raiser, Yu P., <u>Physics of Shock Waves and High-Temperature Hydrodynamics Phenomena</u>, Vol. 1, p. 259, Academic Press, New York, 1966.

APPENDIX A

UV/VISIBLE LASER EFFECTS

1. INTRODUCTION

While a great deal of work has been done on laser effects
with pulsed infrared lasers,[1] only recently have UV lasers of
suitable energy levels been developed.[2] In the IR, the inter-
action between a pulsed laser and an aluminum surface in air is
dominated by the formation of a plasma, which totally absorbs
the laser energy. The plasma then reradiates a large fraction of
this energy in the UV. Since aluminum is a very good reflector
in the IR, but a good absorber in the UV, this leads to higher
surface coupling than would be expected if the plasma were absent.
In addition, the plasma generates a significant impulse level on
the target by remaining at high pressure for a significant period
of time. With a UV laser, where the photons are much more ener-
getic and where the basic absorptivity of the surface is higher,
the phenomenology may be different.

We measured the thermal coupling of the pulsed KrF/XeF laser
beam to the target and the impulse generated by the laser using
standard techniques[1] (thermocouples and a pendulum, respectively).
The laser and its diagnostics have been described previously.[2]
For KrF experiments it was operated so as to produce pulses of
500 nsec pulse length and up to 20 J energy. A stable resonator

---

1. McKay, J.A., Schriempf, J.T., Cronburg, T.L., Eninger, J.E.,
   and Woodroffe, J.A., Appl. Phys. Lett. 36, 125 (1980).

2. Jacob, J. H., Hsia, J. C., Mangano, J. A., and Rokni, M.,
   J. Appl. Phys. 50, 5130 (1979).

was used, leading to multi-mode output. The fluence level on the targets was varied by locating targets at different positions, relative to a 50 cm focal length lens. The environment was 1 atm air. The minimum spot diameter used was 0.5 cm. The targets were made of 2024-T3 aluminum, 0.05 cm thick (0.020 in.). The pendulum weight was 7.5 g.

For most of the XeF work, a laser pulse length of 600 nsec was used, although some of the impulse coupling data were obtained using pulse lengths up to 1.5 μsec. Output energies up to 7 J were used. The XeF experiments were performed in a vacuum chamber which was placed at the focal point of the 50 cm focal length lens which focussed the laser output. By moving the lens, the spot size on our targets was varied between ~0.04 and ~0.6 cm^2. We used a pendulum with a 15 cm arm and a mass of ~1.2 gm.

2. RESULTS

Figure A-1 shows the KrF results for thermal coupling. We have plotted the fraction of the incident laser energy that remains in the target after the pulse is over versus incident fluence. The advantage of this procedure is that the energy out of the laser is known more accurately than the fluence distribution over the spot. As long as the spot is not too small, the difference will be small between coupling measured in this way, and that measured by relating the temperature rise in the center of the spot to the fluence incident on the center of the spot. The fraction of energy coupled is in the range 40%. The low flux room temperature

60
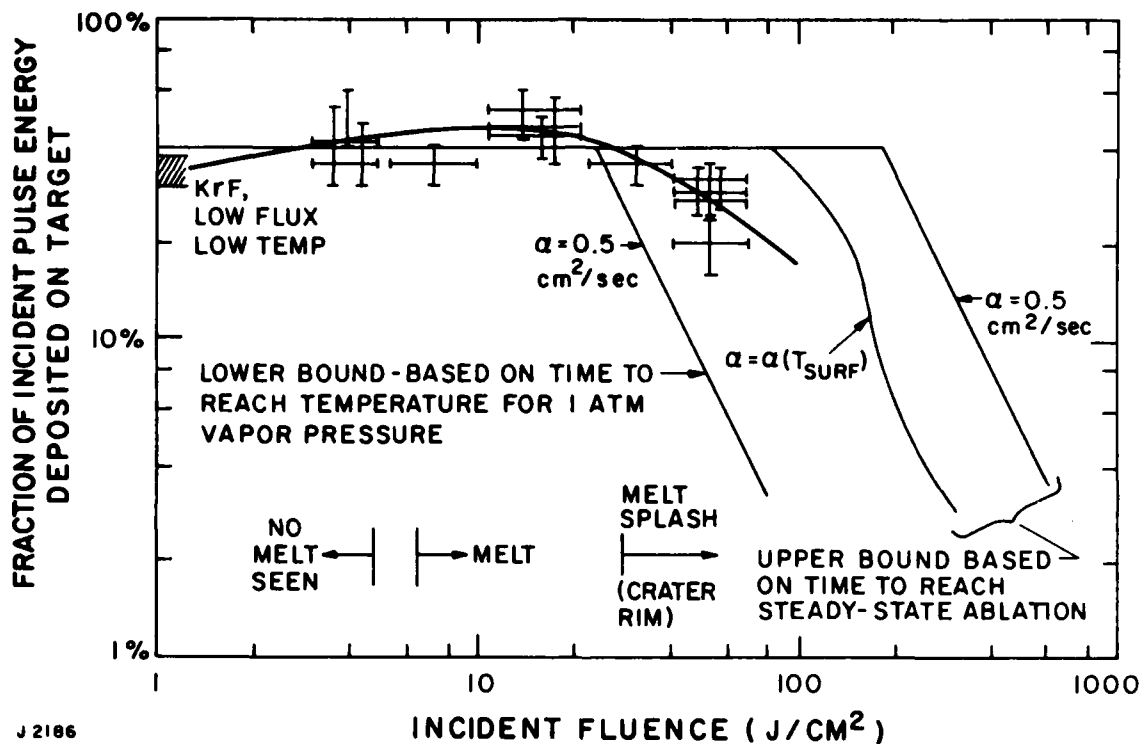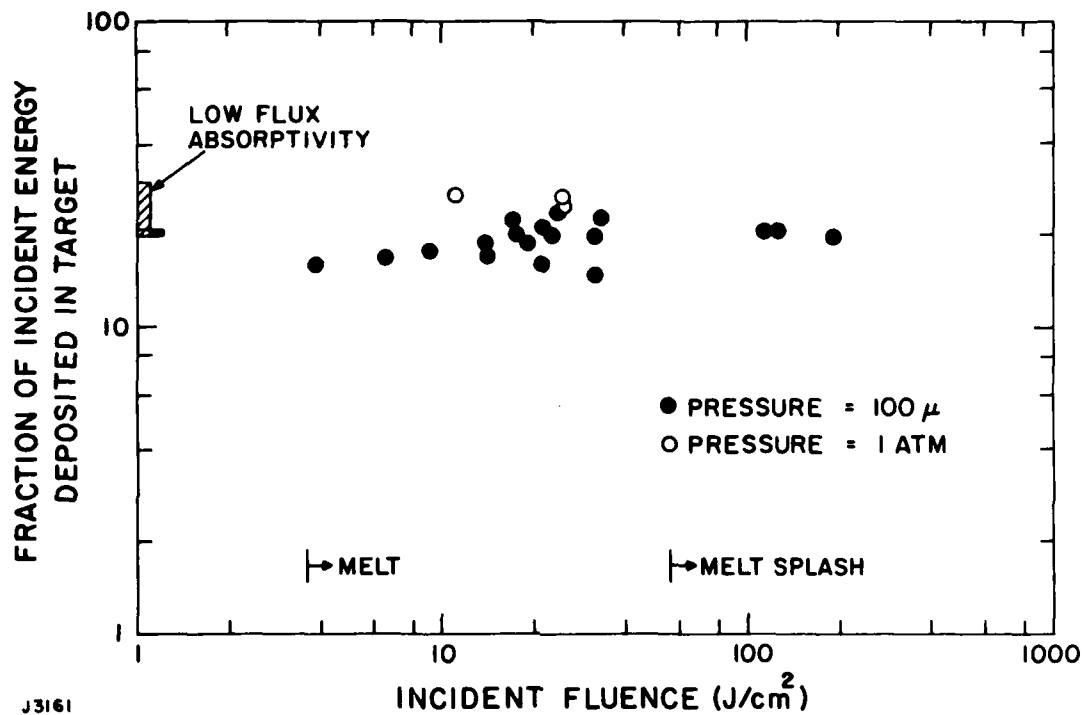
Figure A-1   Thermal Coupling of KrF Laser to Bare Aluminum.
Pressure: 1 atm pulse energy: 7-10 J pulse length:
0.5 μsec. The heavy line is a guide to the eye
through the data. The light lines are analytical
bounds on the coupling, based on 40% inherent ab-
sorptivity; α is the thermal diffusivity of aluminum.

absorptivity at this wavelength is typically 30-40%.[3] The phenomenological behavior is shown at the bottom of the plot; melt is visible on the targets at fluences $\gtrsim 6$ J/cm^2; at fluences $\gtrsim 20$ J/cm^2, a crater rim is observed, indicating that melt has been splashed to the edge of the spot, but no mass loss from the target was observed (to a level of 0.2 mg) at any fluence. We have also shown in Figure A-1 two theoretical bounds on the coupling, both related to energy removal by metal vapor flow from the target surface. A lower bound can be obtained by assuming that as soon as the 1 atm vapor pressure is achieved, all of the extra incident energy is carried off by the vapor. An upper bound is obtained by assuming that no energy is carried off until steady-state vaporization is achieved (at a much higher vapor pressure aned surface temperature). The value for steady-state temperature was obtained using the model of Ref. 4. The data can be seen to fall off between the two bounds.

Figure A-2 contains the results of the thermal coupling measurements with XeF. We have plotted the fraction of the incident laser energy that remains in the target after the pulse is over versus the incident fluence. The thermal coupling at moderate fluences is $\sim 20\%$. The low fluence limit of $\sim 22\%$ indicated in this figure was obtained from one of our samples after polishing using a Cary 17 Spectrophotometer. This is in

---

3. Touloukian, Y. S. and Ho, C. Y., eds., Thermophysical Properties of Selected Aerospace Materials, (TEPIAC?CINDAS, Purdue University) (1976).

4. Knight, C., AIAA J. 17, 519 (1979).

Figure A-2   Thermal Coupling of XeF to an Aluminum Surface as
a Function of Incident Fluence. A pulse length of
0.6 s and energies up to 7 J were used. Results in
air at 0.1 torr (dots) and 760 torr (open circles)
are shown. The low fluence absorptivity was obtained
from Ref. 3.

agreement with previously reported values for 2024 aluminum of 20-30%.[3] While most of our data were obtained at a background pressure of 0.1 torr, three shots were taken at atmospheric pressure and are indicated in Figure A-2. Both in air and vacuum, at fluences $\gtrsim 4$ J/cm^2, melt was observed on the surface of our targets. For fluences $\gtrsim 100$ J/cm^2 a "crater rim" caused by melting aluminum being splashed to the edges of the laser spot was observed. It should be noted that no melt splash was present for fluences up to 30 J/cm^2, even though melt splash was observed with KrF in air at fluences > 20 J/cm^2. This is consistent with the measured thermal coupling.

All of our measurements were obtained at fluence levels ($\gtrsim 4$ J/cm^2) and flux levels ($\gtrsim 7$ MW/cm^2) sufficient to cause surface melt, thereby causing our samples to behave like polished surfaces. This is consistent with the fact that our measured absorptivities are similar to the low fluence absorptivity of a polished surface.[3] However, for very small incident fluences where no surface melting occurs, the roughness of the target surface may cause an increase in the observed absorptivity.

Figure A-3 shows the results for impulse generated by the KrF laser versus incident fluence. We have plotted impulse on the left-hand side and a coupling coefficient C for impulse versus energy on the right-hand side. At 0.3 J/cm^2, no surface flash or pendulum motion were observed. For all the other points, a surface flash was seen (even though at the lower fluences surface melt was not apparent). In the infrared, it is well
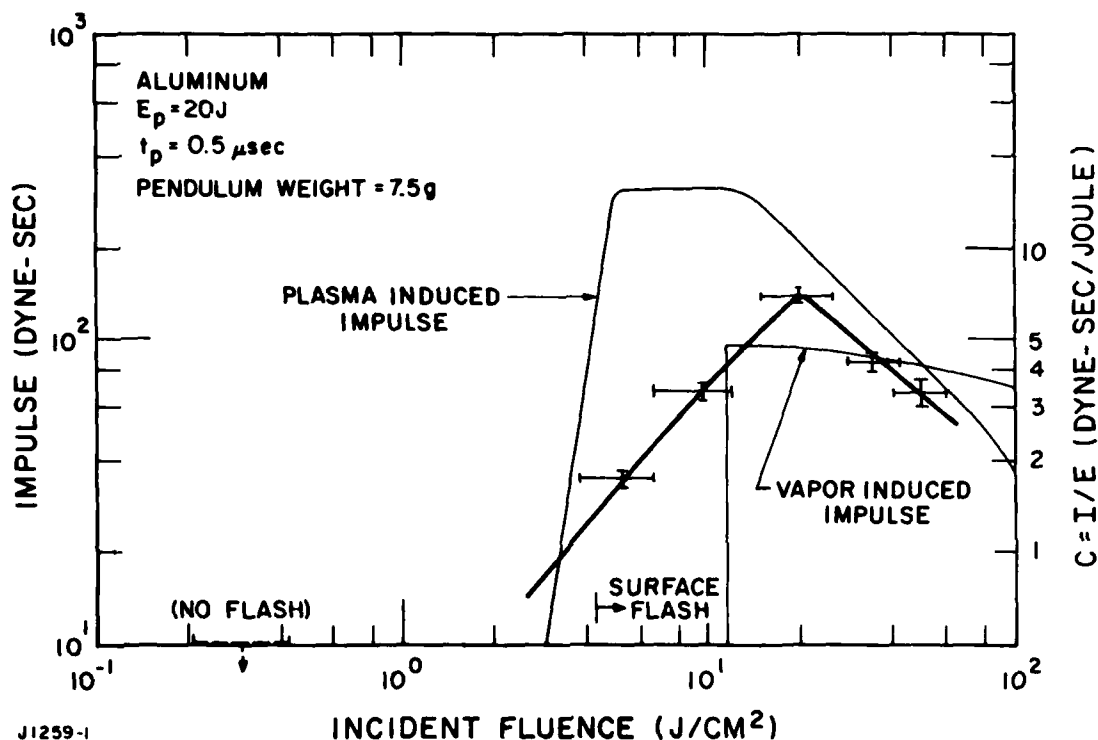
64

J1259-1

Figure A-3   Impulse Produced by a KrF Laser on Aluminum. Pres-
                sure: 1 atm pulse energy: 20 J, pulse length: 0.5
                μsec. The heavy line is a guide to the eye through
                the data. The light lines are calculations for
                plasma (laser supported detonation wave) impulse
                with an ignition threshold of 3 J/cm^2 and vapor
                induced impulse with 40% inherent absorptivity.

known that a surface plasma can form which can lead to high
thermal coupling and to significant pressure and impulse levels.
We have taken a model developed for plasma impulse coupling by
an IR laser via a laser supported detonation (LSD) wave[5] and
used it without modification for the fluxes and pulse length of
these experiments, assuming a plasma ignition threshold level of
3 J/cm^2. The calculation is shown on Figure A-3. For comparison,
we have also done a calculation for the impulse caused by steady-
state bulk vaporization recoil.[4,6] The timescale for steady-
state vaporization to be reached is longer than the pulse length
for the entire range of experimental fluences. The vaporization
calculation is based on a steady-state condition being reached,
and is thus an upper bound. This becomes a more accurate descrip-
tion as the fluence increases towards 10^2 J/cm^2. The general
levels of the two calculations are in the right range, though
neither is accurate, suggesting that a more detailed model of the
physics will be required.

Figure A-4 shows the results of our impulse coupling
measurements for XeF. The impulse coupling coefficient (dyne-
sec/joules) is plotted versus incident fluence. Results for
background pressures of 0.1 and 2 torr are shown; there is no
discernable difference between the two sets of results. Measure-
ments to the impulse coupling coefficient were also performed at

5. Reilly, J. P., Ballantyne, A., Woodroffe, J. A., AIAA. J. 17,
    1098 (1979).

6. Shui, V. H., Young, L. A., Reilly, J. P., AIAA J. 16, 649
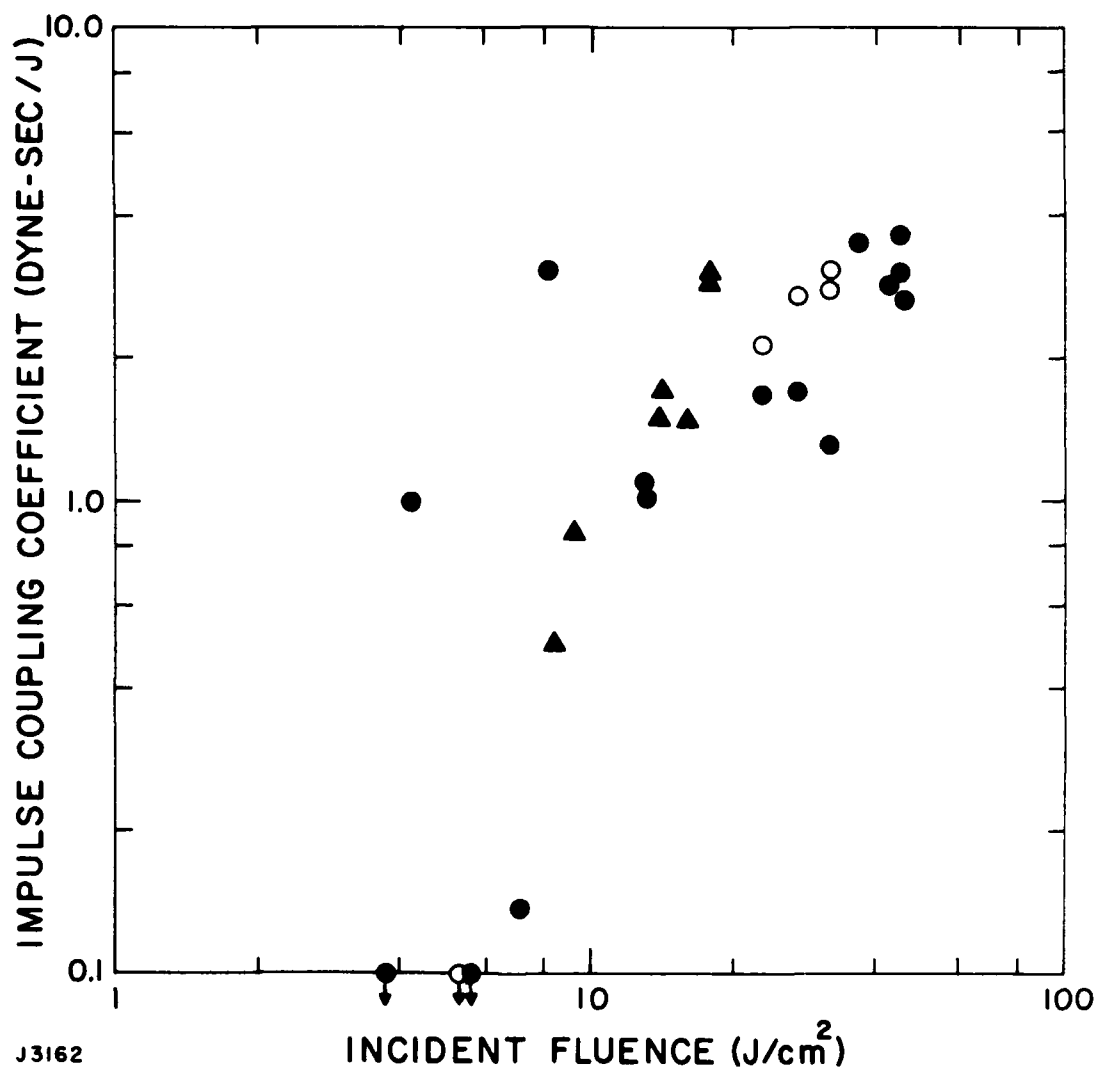   (1978).

Figure A-4   Impulse Coupling Coefficient for XeF to an Aluminum
              Surface as a Function of Incident Fluence.   Energies
              of 0.8-2.0 J were used.

              ● – P = 0.1 torr, τ_p = 1.0-1.4 μsec;

              Λ – P = 0.1 torr, τ_p = 0.5-0.8 μsec;

              o – P =   2 torr, τ_p = 1 μsec

67

atmospheric pressure and 75 torr and these results are given in Figure A-5. Again, the results at 1 atm and 75 torr exhibit similar behavior. It should be .loted that no sudden disappearance of impulse coupling as a function of decreasing fluence was observed. Instead, the pendulum motion gradually decreased as the fluence decreased until at ~ 4 J/cm^2, any motion became too small for us to detect. At all fluences where pendulum motion was observed, a surface flash was also present and, moreover, this surface flash persisted until the fluence was decreased below ~ 2 J/cm^2.

We observed this behavior even though the target surface had been melted by a number of previous shots. We believe it is due to the presence of surface defects. Scans of the surface by SEM, in fact, show a large number of defects on pre-melted surfaces, as well as on "as-received" surfaces.

3. CONCLUSION

In summary, we have observed high thermal coupling of KrF and XeF laser radiation to an aluminum surface ($\sim 40\%$ and $\sim 20\%$, respectively), and the appearance of significant impulse levels at low fluence.
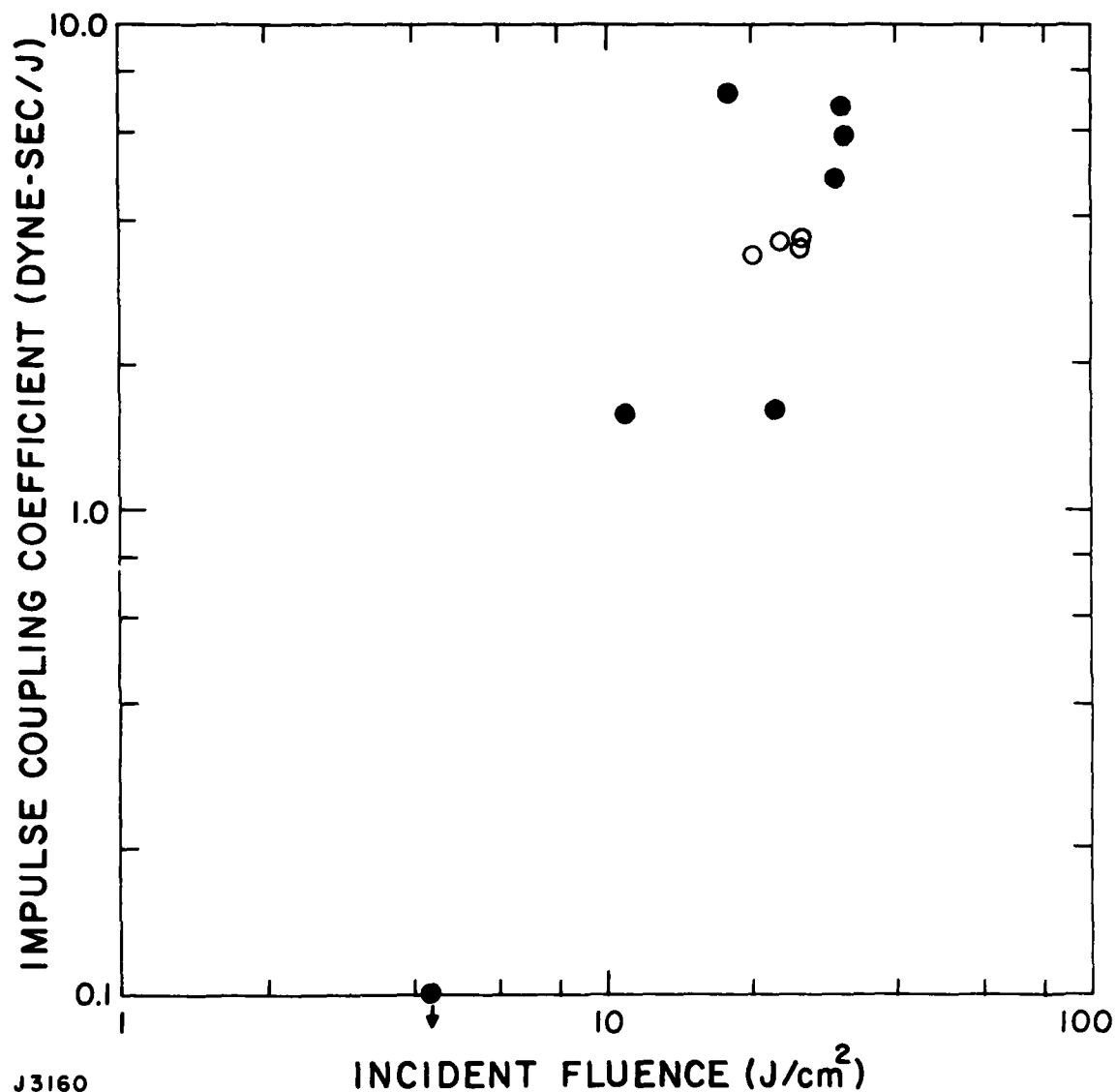
J3160

Figure A-5   Impulse Coupling Coefficient for XeF to an Aluminum
              Surface as a Function of Incident Fluence.   Energies
              of 0.8-1.4 J were used.

● - P = 760 torr, τ_p = 1.0 μsec;

○ - P = 75 torr, τ_p = 1.0 μsec.

69

APPENDIX A

REFERENCES

1. McKay, J.A., Schriempf, J.T., Cronburg, T.L., Eninger, J.E., and Woodroffe, J.A., Appl. Phys. Lett. $\underline{36}$, 125 (1980).

2. Jacob, J.H., Hsia, J.C., Mangano, J.A., and Rokni, M., J. Appl. Phys. $\underline{50}$, 5130 (1979).

3. Touloukian, Y.S. and Ho, C.Y., eds., Thermophysical Properties of Selected Aerospace Materials, (TEPIAC/CINDAS, Purdue University (1976).

4. Knight, C., AIAA J. $\underline{17}$, 519 (1979).

5. Reilly, J.P., Ballantyne, A., Woodroffe, J.A., AIAA J. $\underline{17}$, 1098 (1979).

6. Shui, V.H., Young, L.A. Reilly, J.P., AIAA J. $\underline{16}$, 649 (1978).

DISTRIBUTION LIST FOR FINAL TECHNICAL REPORT

Contract No. DAAH01-80-C-1523

Commander, U.S. Army Missile Command, Redstone Arsenal, AL 35809, Attn: DRSMI-RAS/Dr. Haak (1 copy)

Director, Defense Advanced Research Projects Agency, 1400 Wilson Blvd., Arlington, VA 22209, Attn: Program Management (MIS Division) (3 copies)

Defense Technical Information Center, Cameron Station, Alexandria VA 22314 (2 copies)

Commander, U.S. Army Missile Command, Redstone Arsenal, AL 35809, Attn: DRSMI-RPR (1 copy)